Chapter 14
A Hydromechanical Model for Lower Crustal Fluid Flow

J.A.D. Connolly and Y.Y. Podladchikov

Abstract Metamorphic devolatilization generates fluids at, or near, lithostatic pressure. These fluids are ultimately expelled by compaction. It is doubtful that fluid generation and compaction operate on the same time scale at low metamorphic grade, even in rocks that are deforming by ductile mechanisms in response to tectonic stress. However, thermally-activated viscous compaction may dominate fluid flow patterns at moderate to high metamorphic grades. Compaction-driven fluid flow organizes into self-propagating domains of fluid-filled porosity that correspond to steady-state wave solutions of the governing equations. The effective rheology for compaction processes in heterogeneous rocks is dictated by the weakest lithology. Geological compaction literature invariably assumes linear viscous mechanisms; but lower crustal rocks may well be characterized by non-linear (power-law) viscous mechanisms. The steady-state solutions and scales derived here are general with respect to the dependence of the viscous rheology on effective pressure. These solutions are exploited to predict the geometry and properties of the waves as a function of rock rheology and the rate of metamorphic fluid production. In the viscous limit, wavelength is controlled by a hydrodynamic length scale δ, which varies inversely with temperature, and/or the rheological length scale for thermal activation of viscous deformation l_A, which is on the order of a kilometer. At high temperature, such that $\delta < l_A$, waves are spherical. With falling temperature, as $\delta \to l_A$, waves flatten to sill-like structures. If the fluid overpressures associated with viscous wave propagation reach the conditions for plastic failure, then compaction induces channelized fluid flow. The channeling is caused by vertically elongated porosity waves that nucleate with characteristic spacing δ. Because δ increases with falling temperature, this mechanism is amplified towards the surface. Porosity wave passage is associated with pressure

J.A.D. Connolly (✉)
Department of Earth Sciences, Swiss Federal Institute of Technology, Zurich 8092, Switzerland

Y.Y. Podladchikov
Geophysics Institute, University of Lausanne, Lausanne 6617, Switzerland

D.E. Harlov and H. Austrheim, *Metasomatism and the Chemical Transformation of Rock*, Lecture Notes in Earth System Sciences,
DOI 10.1007/978-3-642-28394-9_14,

anomalies that generate an oscillatory lateral component to the fluid flux that is comparable to the vertical component. As the vertical component may be orders of magnitude greater than time-averaged metamorphic fluxes, porosity waves are a potentially important agent for metasomatism. The time and spatial scales of these mechanisms depend on the initial state that is perturbed by the metamorphic process. Average fluxes place an upper limit on the spatial scale and a lower limit on the time scale, but the scales are otherwise unbounded. Thus, inversion of natural fluid flow patterns offers the greatest hope for constraining the compaction scales. Porosity waves are a self-localizing mechanism for deformation and fluid flow. In nature these mechanisms are superimposed on patterns induced by far-field stress and pre-existing heterogeneities.

14.1 Introduction

The volume change associated with isobaric metamorphic devolatilization is usually positive, consequently devolatilization has a tendency to generate high pressure pore fluids. This generality has led to the notion that high fluid pressures are the ultimate cause of metamorphic fluid flow. A simple experiment with a well-shaken bottle of soda pop (i.e., a sweet, carbonated, beverage) demonstrates that this notion is ill conceived. Once the bottle is opened some pop is lost, but, after a short time, flow ceases leaving most of the initial pop in the bottle. In the metamorphic analogy, the bottle is the porous rock matrix and the pop is its pore fluid. How then is this pore fluid expelled? As early as 1911, Goldschmidt (1954) realized that fluid expulsion could only occur if the rock compacts and squeezes the pore fluid out. The compaction process is a form of deformation that, usually, is driven by the weight of the overlying rock. In this case, the downward flow of the rock matrix, in response to gravity, is responsible for the upward flow of the less dense pore fluid. Compaction driven fluid flow is complex because it is inseparable from rock deformation and because the hydraulic properties that limit fluid flow through the rock matrix, such as permeability and porosity, are dynamic. This chapter outlines a physical model for the compaction process in the Earth's lower crust. While the specifics of this chapter are of direct relevance only to continental crust, the concepts apply to oceanic crust as well.

Metamorphic devolatilization usually results in a significant decrease in the volume of the residual solid, e.g., serpentine dehydration causes a reduction in the solid volume in excess of 10%. Without compaction, this change in volume would be preserved as grain-scale porosity. Thus, the near absence of grain-scale porosity in exhumed metamorphic rocks (Norton and Knapp 1977) is unequivocal evidence for irreversible compaction. Despite this evidence, irreversible compaction is almost universally disregarded in quantitative models of metamorphic fluid flow. This neglect is reasonable provided the fluid flow of interest occurs on a short time scale compared to the time scale for compaction. Because viscous compaction is thermally-activated, neglecting compaction becomes more problematic, but not

necessarily invalid, with increasing metamorphic grade. Likewise, although compaction is an appealing explanation for ubiquitous evidence of high fluid pressure during metamorphism (e.g., Etheridge et al. 1984; Sibson 1992; McCuaig and Kerrich 1998; Simpson 1998; Cox 2005; Rubinstein et al. 2007; Peng et al. 2008; Scarpa et al. 2008; Padron-Navarta et al. 2010), high fluid pressures cannot be explained unless metamorphic systems are poorly drained. However, if metamorphic systems are poorly drained, high fluid pressures may simply be a consequence of ephemeral fluid production. This argument is not brought forward to justify the neglect of compaction in modeling metamorphic fluid flow, but rather to emphasize that the conditions at which compaction becomes important are uncertain. An intriguing set of observations (Young and Rumble 1993; van Haren et al. 1996; Graham et al. 1998) indicate that localized fluid-rock interaction at amphibolite-facies conditions occurred on a time scale of 10^3–10^5 y during much longer (~10^7 y) regional metamorphic events. An explanation for the limited duration of fluid-rock interaction is that compaction sealed the rocks on the 10^3–10^5 y time scale. Transiently high metamorphic permeability on similar time scales (Ingebritsen and Manning 2010) and geophysically observable sub-Himalyan densification on a time scale of < 1 My at eclogite facies conditions (Hetenyi et al. 2007) provide additional evidence that compaction is an efficient process at moderate metamorphic temperatures. Compaction is synonymous with fluid expulsion, thus if metamorphic fluid flow is compaction dominated, exotic fluid sources and crustal scale fluid recirculation should have limited impact on the metamorphic fluid budget (Walther and Orville 1982). That metamorphic fluid fluxes, inferred from field studies (e.g., Ferry 1994; Skelton 1996; Wing and Ferry 2007; Manning and Ingebritsen 1999), are comparable to the vertically integrated metamorphic fluid production (Walther and Orville 1982; Yardley 1983; Connolly and Thompson 1989) is suggestive that metamorphic flow regimes are indeed compaction dominated.

The assumption of classical metamorphic petrology, that fluid pressure is equal to the total pressure, implies that rocks compact in response to negligible effective pressure, i.e., that rocks have no strength. In this limit, compaction driven flow of a low-density fluid can only be upward (Walther and Orville 1982). A surprising feature of compaction-driven fluid flow in rocks of finite strength is that a perturbation, e.g., a metamorphic devolatilization reaction, to a uniform flow regime induces a regime in which fluid flow occurs by the propagation of domains of fluid-filled porosity (Richter and McKenzie 1984; Scott and Stevenson 1986; Suetnova et al. 1994; Wiggins and Spiegelman 1995; Connolly 1997). The properties of these domains closely approximate steady-state wave solutions to the equations that describe fluid flow in compacting media (Barcilon and Richter 1986; Barcilon and Lovera 1989). In this porosity wave propagated flow regime, while the overall tendency is to drive fluid upward or, in the presence of tectonic stress, toward low mean stress (Connolly and Podladchikov 2004), lateral fluid flow occurs on the time and spatial scales of the steady-state waves. In a homogeneous crust that is not subject to tectonic forcing, such waves would be the primary mechanism of metamorphic fluid flow. This idealization is far from reality, but

the steady-state wave solutions define background patterns upon which the effects of lithological heterogeneity and tectonic deformation are imposed. Consequently, the spatial and temporal scales of the compaction process limit the extent to which perturbations may influence the idealized compaction-driven flow regime. For example, a transient shear zone may induce both lateral and downward fluid flow (Austrheim 1987; Sibson 1992), but it can only do so on time and spatial scales shorter than those for compaction (Connolly 2010). Understanding the time and length scales of steady-state wave solutions to the compaction equations is thus essential to understanding lower crustal fluid flow, even if the flow is not dominated by compaction.

The physical explanation for the existence of porosity waves requires only an elementary understanding of the driving forces and constitutive relations that govern fluid flow, but the derivation of the steady-state solutions involves cumbersome math (Barcilon and Richter 1986; Barcilon and Lovera 1989). The intent here is to avoid this math, which is summarized in the Appendix, and to focus on the physical constraints that influence the steady-state solutions. The first part of this Chapter reviews the rheological and hydraulic concepts relevant to the compaction process. Large scale modeling of metamorphic fluid flow inevitably invokes a steady-state hydraulic regime to define the pre-metamorphic state. This initial steady state is critical to model outcomes because it determines the response of the system to the metamorphic perturbation. Unfortunately, because metamorphism is the most probable source of lower crustal fluids, the assumption of an initial steady state leaves much to be desired. In truth, in the modeling of metamorphic fluid flow, less is known about the initial state than is known about the metamorphic state. The second part of this Chapter draws attention to the uncertainties inherent in defining the pre-metamorphic lower crustal hydraulic regime, and the final part details the expected scales and patterns of compaction-driven flow as function of initial conditions and rheology.

14.2 Compaction Pressures and Rheologic and Hydraulic Constitutive Relations

In compaction problems, fluid is distinguished from the solid phase(s) by its shear strength; specifically the fluid is defined as a phase that cannot support deviatoric stress. This definition has the implication that on the time scale relevant for compaction, fluid pressure is uniform throughout the connected porosity at the scale of the solid grains and is independent of the solid pressure. The term porosity is used here to mean only this connected porosity; rocks may contain porosity that is not interconnected, but because this porosity does not influence fluid flow it is of little interest. Further, it is assumed that the porosity is always filled by fluid, i.e., porosity is simply the volume fraction of fluid in the solid matrix. Although the word porosity conjures up an image of grain-scale structures, it may apply to

substantially larger features, such as fractures, provided these features are small in comparison to the length scale for fluid flow.

Compaction is formally the change in porosity caused by dilational (volume changing) strain of a solid matrix, i.e., the isotropic component of the strain tensor. It follows from the Curie principle that compaction can only be a direct function of invariant characteristics of the stress state. From Terzhaghi's effective stress concept, the simplest invariant is the effective pressure, i.e., the difference between total pressure and fluid pressure, which is assumed here to be the sole cause of compaction. The total pressure can be decomposed into components due to the fluid and solid as

$$p = (1 - \phi)p_s + \phi p_f \tag{14.1}$$

where ϕ is porosity and subscripts s and f denote solid and fluid, respectively (see Table 14.1 for notation). Making use of Eq. 14.1, and observing that mean stress, $\bar{\sigma}$, and pressure are formally equivalent, effective pressure is

$$p_e \equiv \bar{\sigma} - p_f = (1 - \phi)(p_s - p_f). \tag{14.2}$$

Because high fluid pressures may lead to negative effective pressures, it is sometimes convenient to describe compaction processes in terms of fluid overpressure, which is defined here as $-p_e$.

Darcy's law (e.g., McKenzie 1984) relates the volumetric fluid flux relative

$$\mathbf{q} = -(1 - \phi)\frac{k}{\mu}(\nabla p_f - \rho_f g \mathbf{u}_z) \tag{14.3}$$

through a porous matrix to the difference between the actual fluid pressure gradient and the hydrostatic pressure gradient of the fluid ($\rho_f g \mathbf{u}_z$), where k is the hydraulic permeability of the solid matrix, ρ_f and μ are the density and shear viscosity of the fluid, and $\mathbf{u}_z$ is a downward directed unit vector. It is often useful to characterize the dynamics of fluid flow by the macroscopic velocity, $\mathbf{v}$, of the fluid rather than flux. As the fluid flux is the product of the fluid velocity and porosity, any expression in terms of flux can be converted to one in terms of velocity via

$$\mathbf{v} = \mathbf{q}/\phi \tag{14.4}$$

Fluid flux is a vector, which is typically negative (upward) for a downward directed depth coordinate. This is a potential source of confusion in that a large upward flux is, numerically, less than a small flux. To minimize such confusion, the magnitude of a vectorial quantity, indicated by italics (e.g., q for flux $\mathbf{q}$ and v for velocity $\mathbf{v}$), is used when direction is evident. Darcy's law relates flux to pressure gradients rather than pressure. This has the implication that a high-pressure fluid need not flow provided its pressure gradient is hydrostatic.

Table 14.1 Frequently used symbols

Symbol	Meaning
A	Coefficient of viscous flow, Eqs. 14.11 and 14.12
c_ϕ	Geometric and grain-size dependent factor in the permeability function, Eq. 14.17
c_σ	Geometric factor in the compaction rate function, Eq. 14.16
D	Pre-exponential term in Arrhenius dependence of A, Eqs. 14.12 and 14.14
e	Base of natural logarithms (2.718...)
g	Magnitude of gravitational acceleration
k; k_0	Permeability, Eq. 14.17; background value
l_A	Viscous e-fold length, Eq. 14.15
n_ϕ	Porosity exponent in the permeability function, Eq. 14.17
n_σ	Stress exponent in the viscous flow law, Eq. 14.11
$O(n)$	Literally, "of the order of magnitude of n"
p; p_e; p_f; p_s	Total pressure, Eq. 14.1; effective pressure, $p - p_f$, Eq. 14.2; fluid pressure; solid pressure
$\mathbf{q}$; q; q_0;$\bar{q}$	Fluid flux, Eqs. 14.3, 14.5, 14.8, and 14.37; fluid flux magnitude; background value; time-averaged value
q_e	Time-averaged fluid flux (magnitude) associated with a 1-d wave, Eq. 14.25
Q	Activation energy for viscous deformation of the solid matrix
R	Universal gas constant
R	Viscosity contrast
T	Temperature, K
$\mathbf{u}_z$	A downward directed unit vector
V_e; V_e^{1d}	Fluid volume associated with a wave, Eq. 14.27; 1-d volume, Eq. 14.26
v; v_0; v_ϕ	Fluid speed; background value; wave speed, Eq. 14.56
z	Depth coordinate, positive downward
$\dot{\varepsilon}$	Shear strain rate, Eq. 14.11
$\dot{\varepsilon}_\phi$	Compaction rate, Eq. 14.16
δ; δ_d	Viscous compaction length, Eq. 14.23; decompaction length for decompaction-weakening, Eq. 14.30
$\Delta\rho$; $\Delta\sigma$	$\rho_s - \rho_f$; differential stress
η	Solid shear viscosity
λ	Wavelength
μ	Fluid shear viscosity
ϕ; ϕ_0	Porosity (hydraulically connected); background value
ρ_s; ρ_f	Solid density; fluid density
$\bar{\sigma}$; σ_y	Mean stress (p), Eq. 14.38; tensile yield stress
τ	Compaction time scale, δ/v_0, Eq. 14.24
∇; $\nabla\cdot$	Gradient ($\partial/\partial z$ in 1-d); divergence ($\partial/\partial z$ in 1-d)

In compaction problems, it is useful to reformulate Darcy's law in terms of the effective pressure responsible for compaction as

$$\mathbf{q} = -(1-\phi)\frac{k}{\mu}(\nabla\bar{\sigma} - \nabla p_e - \rho_f \mathbf{g}\mathbf{u}_z). \tag{14.5}$$

For the classical $p = p_f$ metamorphic model (i.e., $\nabla p_e = 0$), this form demonstrates that the direction of fluid flow is a function of the mean stress gradient, which may

be influenced by tectonic processes. These effects complicate discussion because they depend on the specifics of the tectonically-induced stress field. To eliminate this complication, it is assumed that the mean stress gradient is due entirely to the vertical load, i.e., that pressure is lithostatic. Tectonic stress affects the direction of compaction driven flow, but does not affect the compaction mechanism, thus the lithostatic assumption is not essential to any of the phenomena discussed here. Making the additional assumptions that solid density is not strongly variable and that porosity is small (i.e., $1 - \phi \approx 1$), total and effective pressures are

$$p \approx p_s \approx \rho_s g z \tag{14.6}$$

$$p_e \approx \rho_s g z - p_f, \tag{14.7}$$

where ρ_s is the density of the solid matrix and z is depth. Rearranging Eq. 14.7 to give fluid pressure in terms of effective pressure, Darcy's law then simplifies to

$$\mathbf{q} = \frac{k}{\mu}(\nabla p_e - \Delta\rho g \mathbf{u}_z). \tag{14.8}$$

At near surface conditions, fluid pressures are near hydrostatic, i.e., $\nabla p_e \approx \Delta\rho g \mathbf{u}_z$, and small perturbations in pressure can cause fluids to flow in any direction. This regime is often referred to as one of normal fluid pressure, whereas at conditions of lithostatic fluid pressure, in which case $\nabla p_e = 0$,

$$q = k\Delta\rho g/\mu \tag{14.9}$$

and flux is vertical and essentially controlled by permeability.

Equations 14.3 and 14.4, give the fluid velocity and flux relative to the reference frame of the solid, but in geological compaction problems solid velocities are finite relative to the Earth's surface. It is assumed here that the solid velocity is negligible. This assumption is justified in the small porosity limit (Connolly and Podladchikov 2007). The Appendix provides a more rigorous treatment that does not neglect solid velocity.

14.2.1 Rheology

Just as in the case of non-dilational rheology, the endmember compaction rheologies are elastic, plastic, and viscous. Strictly elastic, plastic, and viscous describe, respectively, reversible time-independent, irreversible time-independent, and irreversible time-dependent deformation (Hill 1950). In the geological literature these terms, particularly plastic, are often confused with terms such as ductile and brittle that describe deformation style. In geological materials, the origin of ductile behavior is most commonly viscous rheology, but may also be a plastic

mechanism, while brittle deformation is a manifestation of plasticity and is usually localized (Ranalli 1995).

Elastic compaction and fluid expulsion results from both solid (β_s) and fluid (β_f) compressibilities and a peculiar component referred to as pore compressibility that is a property of the fluid–rock aggregate (Gueguen et al. 2004). Although pore compressibility dominates the compaction of poorly consolidated sediments, in rocks with porosities below a few percent, pore compressibilities become comparable to the solid compressibility, which is $O(10^{-11})$ Pa^{-1} (Wong et al. 2004; the notation $O(n)$, which means, literally, "of the order of magnitude of n", is used extensively in this chapter because of our concern with scales based on highly uncertain parameters). Thus, for lower crustal rocks, the elastic compaction caused by a change in effective pressure Δp_e is

$$\Delta\phi/\phi \approx -\beta_s \Delta p_e. \tag{14.10}$$

From Eq. 14.10, a reduction in p_f from lithostatic to hydrostatic conditions at 20 km depth ($\Delta p_e = \Delta\rho g z$) decreases by 0.4% of its initial value. As fluid compressibilities are roughly an order of magnitude greater than solid compressibility at the conditions of the lower crust (Walther and Orville 1982), the net fluid expulsion necessary to effect the pressure drop is only ~4.4% of the fluid mass initially present in the porosity. Thus, at typical lower crustal conditions, elastic dilational strain can be neglected as a mechanism for lower crustal fluid expulsion. In this regard it is important to distinguish fluid expulsion from fluid flow as, particularly in the non-compacting limit, thermoelastic expansivity of the fluid may create pressure gradients responsible for fluid circulation (e.g., Hanson 1997; Staude et al. 2009; Nabelek 2009).

Excepting irreversible phase transformations, viscous and plastic bulk strains in rocks are caused by microscopic shear deformation that eliminates porosity. Plastic rheologies are complex, but fortunately only cataclastic and Mohr-Coulomb plastic rheologies are of relevance here. Cataclasis (Wong et al. 2004), the crushing of grains in response to increasing load, is a well-known phenomenon in sedimentary basins where it gives rise to an exponential decay of porosity with depth (Athy 1930; Connolly and Podladchikov 2000). Crushing is inescapable once stress concentrations approach the ultimate strength of the solid material (Hill 1950), which is itself 10% of the shear modulus of the solid. Thus, the role of cataclastic compaction must be acknowledged once stress concentrations are $O(1)$ GPa. In sedimentary rocks, the requisite stress concentrations are caused by irregular grain contacts. These asperities are gradually eliminated during compaction, leading to strain-hardening. In sediments, this strain-hardening typically limits cataclastic compaction to rocks with porosities in excess of a few percent (Hunt 1990; Powley 1990). Cataclasis is thus unlikely in lower crustal metamorphic rocks unless effective pressures are exceptionally large.

Although brittle failure is usually thought of as a mechanism for accommodating shear strain, positive dilational strain (i.e., dilatancy) is an inescapable consequence of non-associated plastic (brittle) failure. If an imposed differential stress is large in

comparison to the tensile strength of the rock matrix, brittle failure may limit fluid pressure to sublithostatic values (Sibson 2004, cf. Rozhko et al. 2007). Given that rock tensile strengths rarely exceed 50 MPa, and may be near zero, in some circumstances truly lithostatic fluid pressures may only be possible in the absence of significant differential stress, whereupon fluid pressure is limited by hydrofracturing, which occurs when the fluid overpressure exceeds tensile strength.

Viscous compaction is unimportant at surface conditions, but, because it is a thermally activated mechanism, it becomes inevitable with increasing temperature. The viscous rheology of the crust is usually described by a power-law constitutive relationship of the form (e.g., Kohlstedt et al. 1995; Ranalli 1995)

$$\dot{\varepsilon} = A|\Delta\sigma|^{n_\sigma - 1}\Delta\sigma, \tag{14.11}$$

where $\dot{\varepsilon}$ is the strain rate in response to differential stress $\Delta\sigma$, n_σ is the stress exponent, and A is the coefficient of viscous flow. The coefficient A is a temperature dependent material property that may also be sensitive to grain size (e.g., pressure solution creep) and chemical factors (e.g., the chemical potential of oxygen and/or water). These latter dependencies are uncertain and therefore disregarded in large-scale modeling, but the temperature dependence is usually retained and described by the Arrhenius relation

$$A = D\exp\left(\frac{-Q}{\mathrm{R}T}\right), \tag{14.12}$$

where Q is the activation energy for the viscous mechanism, and D is a material property that is independent of temperature. To provide a simple model for the viscous rheology of the lower crust, D is parameterized here in terms of the strain-rate, stress, temperature, and depth of the brittle-ductile transition, i.e., the depth at which viscous mechanisms become capable of accommodating tectonic strain rates (Kohlstedt et al. 1995). In compressional settings, at this depth, z_{BD}, assuming $\sigma_2 = (\sigma_1 + \sigma_3)/2$ and the hydrostatic fluid pressure, the Mohr-Coulomb rheology of the upper crust defines the differential stress as (Petrini and Podladchikov 2000)

$$\Delta\sigma_{\mathrm{BD}} = gz_{\mathrm{BD}}\frac{\rho_{\mathrm{f}}(3\sin\theta - 1) - 2\rho_{\mathrm{UC}}\sin\theta}{\sin\theta - 1} \tag{14.13}$$

where, by Byerlee's law, the internal angle of friction $\theta = \pi/6$ (Ranalli 1995) and ρ_{UC} is the density of upper crustal rock. For $\rho_{\mathrm{f}}/\rho_{\mathrm{UC}} = 0.3$, Eq. 14.13 simplifies to $\Delta\sigma_{\mathrm{BD}} = 1.7\rho_{\mathrm{UC}}gz_{\mathrm{BD}}$. Substituting this estimate for $\Delta\sigma$ in Eq. 14.11 and making use of Eq. 14.12

$$D = \frac{\dot{\varepsilon}_{\mathrm{BD}}}{(1.7z_{\mathrm{BD}}\rho_{\mathrm{UC}}g)^{n_\sigma}}\exp\left(\frac{Q}{\mathrm{R}T_{\mathrm{BD}}}\right). \tag{14.14}$$

The validity of this parameterization hinges on whether Eqs. 14.11 and 14.12 provide an adequate description of the ductile mechanism, but does not require or imply that metamorphism occurs in a compressional tectonic setting or that the brittle-ductile transition during metamorphism occurs at the conditions chosen for the parameterization. Activation energies and stress exponents are relatively well known from rock deformation experiments. Typical values for crustal rocks are in the range $n_\sigma = 2.5 - 4$ and $Q = 150 - 400$ kJ/mol. The depth, temperature, and strain rate at the base of the seismogenic zone, which is usually considered to correspond to the brittle portion of the crust (Sibson 1986; Scholz 1988; Zoback and Townend 2001), are $z_{BD} \approx 3 - 20$ km, $T_{BD} \approx 623 - 723$ K and $\dot{\varepsilon}_{BD} \approx 10^{-12}$ to 10^{-16} s^{-1}, but these ranges are not independent due to autocorrelation (Liotta and Ranalli 1999; Ranalli and Rybach 2005). The values $n_\sigma = 3$, $Q = 250$ kJ/mol, $T_{BD} = 623$ K, $\dot{\varepsilon}_{BD} = 10^{-15}$ s^{-1}, $z_{BD} = 15$ km, and $\rho_{UC} = 2{,}700$ kg/m^3 are taken here to represent a plausible, but by no means unique, condition for the brittle-ductile transition.

It is often useful to characterize the variation in viscous rheology due to the increase in temperature with depth in terms of a depth interval rather than a temperature change. For this purpose, differentiation of Eq. 14.12, with respect to depth, yields the desired measure

$$l_A = A \Big/ \frac{\partial A}{\partial z} = \frac{RT^2}{Q \frac{\partial T}{\partial z}}, \tag{14.15}$$

which is the change in depth necessary to increase strain rates by a factor of e (2.718...). For the parameter choices specified above, the viscous e-fold length l_A is $O(1)$ km at the conditions of lower crustal metamorphism (Fig. 14.1). In the upper crust, pressure solution gives rise to a linear viscous ($n_\sigma = 1$) rheology that is characterized by activation energies in the range 20 –40 kJ/mol (Rutter 1983; Spiers and Schutjens 1990; Shimizu 1995; Connolly and Podladchikov 2000). From Eq. 14.15, such small activation energies increase l_A by an order of magnitude, implying a weak depth dependence that is inconsistent with the restricted depth range and temperature dependence of the seismogenic zone (Sibson 1986; Scholz 1988; Ranalli and Rybach 2005). Thus, it is unlikely that pressure solution is the viscous mechanism responsible for the brittle-ductile transition.

For a material that deforms by viscous creep according to Eq. 14.11, the compaction rate (Wilkinson and Ashby 1975) is

$$\dot{\varepsilon}_\phi = \frac{1}{\phi}\frac{\mathrm{d}\phi}{\mathrm{d}t} = -c_\sigma \frac{(1-\phi)^2}{\left(1-\phi^{1/n_\sigma}\right)^{n_\sigma}} A |p_e|^{n_\sigma - 1} p_e \approx -c_\sigma A |p_e|^{n_\sigma - 1} p_e, \tag{14.16}$$

where the approximate form, which is adopted hereafter, applies in the small-porosity limit. The geometric factor $c_\sigma = n_\sigma^{-n_\sigma}(3/2)^{n_\sigma+1}$ follows rigorously only for spherical pore geometry. At the level of accuracy required here, this geometric

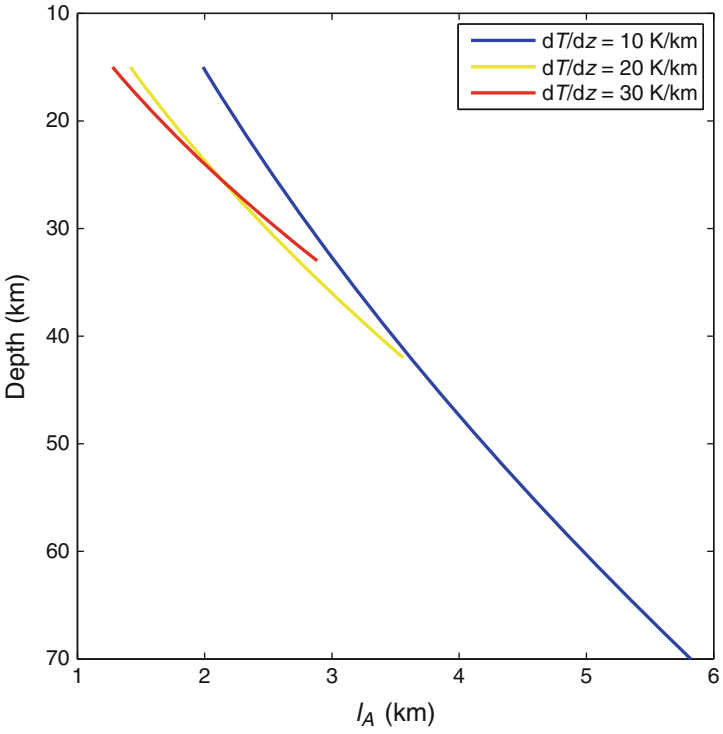

Fig. 14.1 The viscous e-fold length l_A is the characteristic length scale for variation in the ductile rheology of the lower crust with depth due to thermal activation (Eq. 14.15). For a given stress, strain rates increase 10-fold over a depth interval $\Delta z = 2.3\ l_A$. The viscous e-fold length is computed for the indicated geotherms, a reference temperature of 623 K at 15 km depth, and an activation energy of $Q = 250$ kJ/mol. Experimentally determined activation energies for dislocation creep in silicate minerals are in the range 135–400 kJ/mol (e.g., Paterson and Luan 1990; Ranalli 1995). Variation within this range affects l_A by less than a factor of two

assumption is an unimportant source of variability. For the specific case of $n_\sigma = 3$, $c_\sigma = 3/16$.

The dependence of the viscous compaction rate on effective pressure has a number of implications for compaction processes during metamorphism. Most notably the viscous mechanism cannot operate at the $p_\mathrm{f} = p$ condition generally assumed in metamorphic petrology. Thus, dilational strain, caused by a metamorphic reaction that initiates at $p_\mathrm{f} = p$, must be accommodated by elastic mechanisms until the induced stresses become large enough to activate viscous or plastic deformation. As these elastic strains are insignificant, during this incipient stage metamorphism is effectively isochoric rather than isobaric.

The assumption that the viscous mechanism is non-linear is not essential to any subsequent argumentation; it is adopted because it is widely accepted and general. Relations for the special case of linear viscous rheology are obtained from the relations for the non-linear case by observing that, when $n_\sigma = 1$, viscosity is $1/(3A)$. Both

compaction and macroscopic shear deformation are accomplished by microscopic shear. Thus, if a rock is simultaneously subject to both modes of deformation, then they must be accommodated by the same microscopic mechanism. This mechanism is determined by the largest of the stresses responsible for the deformation, $|\Delta\sigma|$ or $|p_e|$, with the result that, if the stresses are of different magnitude, the viscous response to the inferior stress is approximately linear and determined by effective viscosity resulting from the deformation induced by the superior stress. Regardless of magnitude, far-field tectonic stress facilitates compaction by lowering the effective viscosity of the solid matrix (Tumarkina et al. 2011).

14.2.2 Permeability

Although the hydraulic permeability of rocks is extraordinarily variable, it is well established from both theoretical studies and empirical observation (Wark and Watson 1998; Xiao et al. 2006) that the permeability of a given rock will vary as a strong function of its connected porosity. Typically, a power-law relationship is assumed such that if the permeability is k_0 at porosity ϕ_0, then

$$k = k_0(\phi/\phi_0)^{n_\phi} = c_\phi \phi^{n_\phi}. \tag{14.17}$$

In its second form, Eq. 14.17 separates the variability of permeability into a component related to its porosity dependence and a coefficient, c_ϕ, which is a function of pore geometry and proportional to the square of the matrix grain size. From analysis of in situ rock permeability, Neuzil (1994) shows that pore geometry and grain size give rise to variations in permeability that span eight orders of magnitude, but that porosity dependence is approximately cubic. This cubic dependence, i.e., $n_\phi = 3$, is adopted here and is predicted from theory irrespective of whether flow is intergranular or fracture controlled (Norton and Knapp 1977; Gavrilenko and Gueguen 1993). Higher exponents are observed in rocks where the degree of hydraulic connectivity varies strongly with porosity (Zhu et al. 1995; Zhu et al. 1999).

14.2.3 Porosity

Given a steady source at depth, it is conceivable that crustal rocks could adjust their permeability to accommodate this flux at lithostatic pressure (Connolly and Thompson 1989). While such a model is problematic, as it implies rocks have no strength, it provides the only basis for assuming that the lower crust has a tendency to evolve towards a state with homogeneous permeability. Unfortunately, this tenuous argument does not extend to porosity given that different lithologies may have the same permeability with drastically different porosities (Neuzil 1994;

Thompson and Connolly 1990). Thus, the only certainty about lower crustal porosity is that it is spatially and temporally variable. An upper bound on lower crustal porosities of $O(10^{-2})$ is provided by the sensitivity of geophysical measurements, but there is no lower bound. On the basis of isotopic diffusion profiles, Skelton et al. (2000) infer background porosities, i.e., the porosity in non-reactive metaphyllites about a metabasite undergoing devolatilization at greenschist facies conditions, in the range of $\phi_0 \sim 10^{-3}$ to 10^{-6}. These are consistent with grain scale porosities in the range 10^{-3} to 10^{-6} measured in exhumed metamorphic rocks (Norton and Knapp 1977). This variability has non-trivial consequences because, discounting the influence of phase changes on intrinsic material properties, the impact of metamorphic reactions on the mechanical properties of the crust is determined by the relative change in porosity via the constitutive relations for permeability (Eq. 14.17) and rheology (Eq. 14.16), e.g., an increase in porosity of 10^{-3} has no significant influence on permeability if it occurs in rocks with an initial porosity of 10^{-2}, but if the initial porosity is 10^{-6}, permeability increases by nine orders of magnitude.

Hydraulically connected porosities of $< O(10^{-2})$ may seem implausible to a reader familiar with percolation theory models of rock permeability (Gueguen and Palciauskas 1994); however such models assume static pore structure. In natural systems, experimental, theoretical, and numerical evidence suggests that textural equilibration may maintain hydraulic connectivity to vanishingly small porosities (Cheadle et al. 2004; cf., Holness and Siklos 2000 and Price et al. 2006). As remarked earlier (Sect. 14.1), the term porosity is used here to denote any hydraulically connected textural features (e.g., cracks) present on a spatial scale significantly less than the, as yet to be defined, compaction length scale. Thus, even if a percolation threshold is relevant to the expulsion process, porosity may take on any value between zero and unity. Evidence for high metamorphic fluid pressures, in combination with low fluid production rates, provides an indirect argument that these porosities are small at the onset of metamorphism. For example, theoretical porosity-permeability models (Connolly et al. 2009) imply that for $O(1)$ mm grain size, the porosity necessary to conduct a plausible $O(10^{-13})$ m/s devolatilization-generated fluid flux (Connolly and Thompson 1989) at lithostatic pressure, is $O(10^{-5})$.

Whether rocks exist that have no hydraulically connected porosity is, to a certain degree, a metaphysical question. Viscous compaction may completely eliminate microcrack connectivity (Gratier et al. 2003; Tenthorey and Cox 2006), but, in texturally equilibrated rocks, grain-scale viscous compaction reduces porosity asymptotically with time. Similarly, chemical cementation and retrograde hydration require the ingress of a fluid phase and therefore are unlikely to completely eliminate porosity. Even seemingly pristine igneous rocks have detectable hydraulic connectivity (Norton and Knapp 1977). Regardless of whether rocks with no hydraulically connected porosity exist, it is certainly possible that devolatilization may occur in a setting in which the surrounding rocks have such low permeabilities that viscous dilational mechanisms become ineffective on the geological time scale. The compaction time scale, discussed subsequently (Sect. 14.5.2), can be used to assess when the viscous mechanism becomes ineffective. In this limit, elastic or

plastic dilational mechanisms must be responsible for fluid flow. Elastic and plastic mechanisms do not require finite hydraulic connectivity and are therefore also capable of explaining fluid flow into truly impermeable rocks (Connolly and Podladchikov 1998), but these mechanisms introduce complexities that are beyond the scope of this Chapter.

14.3 The Lower Crustal Hydrologic Regime

Conventional wisdom holds that continental crust can be divided into two hydrologic regimes, an upper crustal regime in which fluid pressures are near hydrostatic and a lower crustal regime in which fluid pressures are lithostatic (Fig. 14.2a). Direct (e.g., Huenges et al. 1997) and geophysical observations (e.g., Zoback and Townend 2001) confirm the existence of the upper regime and suggest that it can extend to depths of 10–15 km, while fluid inclusion data and deformation styles support the existence of the lower regime, at least during episodes of regional metamorphism (e.g., Etheridge et al. 1984; Sibson 1992; Cox 2005). The observation that fluid overpressures develop at a eustatic compaction front at ~ 3–4 km depth in many sedimentary basins suggests that compaction can establish a steady-state connection between the hydrostatic and lithostatic regimes. However, this steady-state is only possible in conjunction with sedimentation, because sediment burial is necessary to compensate for upward propagation of the compaction front (Connolly and Podladchikov 2000). Given that steady burial is not a characteristic continental process, a steady-state connection between the hydrologic regimes is improbable.

In active metamorphic settings, the transition between hydraulic regimes can be explained by both the compacting and non-compacting limiting cases. In the compacting case, thermally activated viscous compaction reduces permeability to levels at which drainage to the upper crust cannot keep pace with expulsion and/or metamorphic fluid production. This scenario is the basis for the false notion that the transition to lithostatic fluid pressure is coincident with the brittle-ductile transition. Assuming hydrostatic fluid pressures are characteristic of the upper crust, at the brittle-ductile transition the effective pressure responsible for compaction is comparable to the differential stress that drives tectonic deformation (Connolly and Podladchikov 2004). From Eqs. 14.11 and 14.16, the compaction rate at the transition is therefore comparable to the tectonic strain rate. Thus, for a tectonic strain rate of 10^{-15} s^{-1}, compaction at the brittle-ductile transition requires $2.3c_\sigma/\dot{\varepsilon} \sim 388$ My to reduce porosity by an order of magnitude. As this time scale is greater than the time scale for heat-conduction limited metamorphism, compaction at the depth of the brittle-ductile transition is an ineffective means of regulating metamorphic fluid pressure unless metamorphism is coeval with anomalously high rates of tectonic deformation. This generality applies to the expulsion process, but the healing of microcrack controlled permeability in shear zones is an indirect mechanism by which localized compaction at shallow crustal levels, and short time scales, may generate hydraulic seals (Gratier et al. 2003; Tenthorey and Cox 2006). These seals

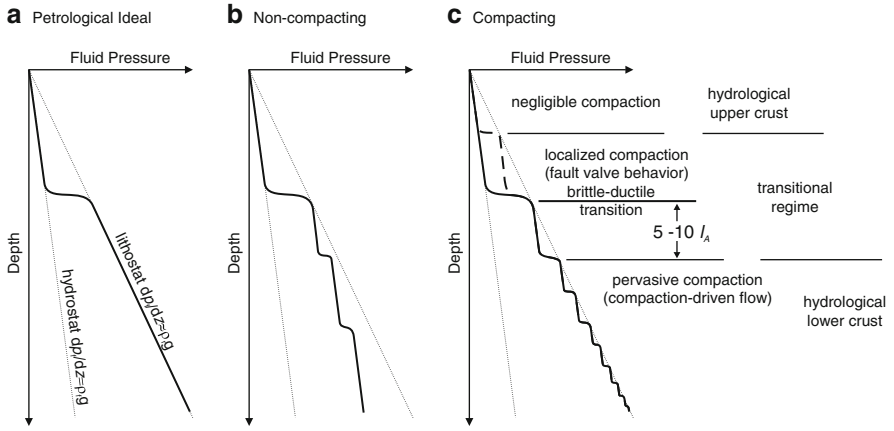

Fig. 14.2 Three models for fluid pressure in the crust. The petrological lithostatic fluid pressure model (**a**) is hydrologically untenable unless permeability is uniform throughout the lower crust and the fluid originates from a steady sub-crustal source. In the non-compacting scenario (**b**) drainage of lower crustal rocks is limited by the least permeable horizon. In the absence of short-term effects related to fluid production, this horizon, i.e., top-seal, would mark the closest approach to lithostatic fluid pressure. Above this horizon fluid pressures would be near hydrostatic. While below the horizon fluid pressure would increase step wise across low permeability seals (Etheridge et al. 1984; Gold and Soter 1985; Hunt 1990; Powley 1990). The superposition of thermally activated compaction on the non-compacting scenario gives rise to three hydrologic regimes (**c**). An upper crustal regime in which faulting maintains such high permeabilities that negligible deviation from hydrostatic fluid pressure is adequate to drive fluid circulation (Zoback and Townend 2001) is limited at depth by the conditions at which localized compaction becomes an effective mechanism for sealing fault-generated permeability (Gratier et al. 2003; Tenthorey and Cox 2006). At greater depths, pervasive compaction and/or metamorphic fluid production may generate transient fluid overpressure that is periodically relieved by faulting (Sibson 1992). At the brittle-ductile transition (i.e., the base of the seismogenic zone) it is improbable that pervasive compaction can keep pace with metamorphic fluid production; thus the transitional hydrologic regime is likely to persist over an interval that extends ~10 l_A below the brittle-ductile transition. Beneath the transitional regime, pervasive compaction is capable of generating hydraulic seals and fluid, if present, is at near lithostatic pressure. Within this lower-most regime, fluid flow is truly compaction-driven. In the absence of fluid production, the tendency of both time and depth is to decrease the wavelength of the fluid pressure compartments resulting in a near-steady regime approximating the petrological ideal. Barring the possibility of a sub-crustal fluid source, the flux in this near steady regime must decrease with depth. Thus the magnitude of the perturbation caused by metamorphic devolatilization to the lower crustal regime is dependent on its depth

may cause fluid overpressure to develop as consequence of local fluid production or deeper expulsion processes (Cox 2005). Viscous compaction rates increase by a factor of e with an increase in depth of $\Delta z \sim l_A$, thus the depth at which compaction operates pervasively on the metamorphic time scale must lie at least several viscous e-fold lengths (Fig. 14.1) below the brittle-ductile transition, but the exact depth is dependent on the rate of metamorphism.

In the non-compacting limit (Fig. 14.2b), lithostatic fluid pressure is generated when metamorphic fluid production overwhelms drainage capacity. A complication

in this scenario is that if fluid pressures are lithostatic throughout the lower crust, then either fluxes are uniform and vertical throughout the lower crust or permeability must be a function of flux rather than porosity. The physical absurdity of either case leads to the conclusion that a heterogeneous permeability structure is the only plausible model for the non-compacting limit. In this case (Fig. 14.2c), fluid pressures cannot be uniformly lithostatic, but approach lithostatic values at low-permeability seals (e.g., Etheridge et al. 1984). The resulting compartmentalized fluid pressure profile is identical to the compartmentalization observed in sedimentary basins (Hunt 1990; Powley 1990). Even in the non-compacting limit, brittle failure permits permeability to increase to accommodate vertical fluxes, but, given the variability of natural permeability with lithology, the permeability of a seal-forming lithology may be orders of magnitude lower than in the intervening rocks. If such seals exist, then, in the absence of metamorphic fluid production, the lower crust may achieve a quasi-steady state with near uniform vertical fluxes in which the closest approach to lithostatic fluid pressure occurs at the uppermost seal. Beneath each seal, Darcy's law requires that the fluid pressure gradient must be nearly hydrostatic, despite large absolute fluid pressures. The time scale for reaching this steady state is dictated by the high-permeability rocks, whereas the effective permeability of the lower crust is defined by the permeability of the top seal. As the vertical flux in this scenario must degrade with time, the number of effective seals must likewise decrease.

As a crustal model, the non-compacting limit has the virtue that it acknowledges the enormous variability of permeability with lithology and it has features that are consistent with both direct and indirect observation. In the former category, results from the Kola deep drilling project suggest the development of fluid compartmentalization at ~8 km depth within the crust (Zharikov et al. 2003). While in the latter category, the existence of permeable horizons with sublithostatic fluid pressure are essential to explain the lateral fluid flow so often inferred in metamorphic studies (Ferry and Gerdes 1998; Wing and Ferry 2007; Staude et al. 2009). Counter-intuitively, the non-compacting scenario is consistent with the idea that the brittle-ductile transition is coincident with the transition in crustal hydrologic regimes if faulting in the brittle domain is responsible for the high permeability of the upper crust (Zoback and Townend 2001).

Thermal activation of viscous compaction dictates the degree to which the compacting or non-compacting scenario is relevant to nature. As the non-compacting limit is broadly consistent with the upper crustal hydrologic regime, it is simplest to develop a conceptual model for the lower crust by considering how depth-dependent viscosity would perturb the non-compacting limit. The primary effect of depth-dependent viscosity would be to reduce the effective pressures sustained within, and therefore the vertical extent of, compartments with depth. Additionally, compaction would provide a source for fluxes, permitting pressurization of seals independently of the top seal. These two effects would lead to a decrease in the wavelength of fluid compartments with depth and lithostatically pressured seals throughout the lower crust, i.e., a pressure profile that would approximate the classical model of lithostatic fluid pressure at depth (Fig. 14.2c).

The absence of any uncontrived steady state for the lower crustal hydrologic regime poses a fundamental limitation to modeling metamorphic fluid flow in that the initial conditions for such models are unconstrained. Thus, by adjusting an arbitrary model parameter, such as the background fluid flux, the modeler has complete control on the impact of metamorphic fluid production on crustal fluid flow. This has the implication that forward modeling of metamorphic fluid flow has little predictive power and that hypothesis testing, based entirely upon modeling, is suspect. The utility of forward models is that they can be used to predict patterns. The comparison of these patterns with natural observations then provides a basis for inverting the parameters and the initial conditions of the metamorphic environments.

14.4 Metamorphic Fluid Production and Dilational Strain

A first order constraint on metamorphic fluid production follows from the observation that between low and high metamorphic grades typical crustal rocks lose ~ 5% of their mass as a consequence of devolitalization (Shaw 1956). For crustal thicknesses of l_c ~ 35–70 km, this implies time-integrated fluxes of the order

$$\hat{q} = \frac{w\rho_r l_c}{\rho_f} \sim O\left(10^4\right)\mathrm{m} \tag{14.18}$$

where w is the weight fraction of the volatiles released during metamorphism. This estimate is comparable to, or greater than, integrated fluxes derived from field studies (e.g., Ferry 1994; Skelton 1996; Wing and Ferry 2007; Staude et al. 2009) suggesting that, at least from a mass balance perspective, there is no necessity to invoke convection cells or exotic fluid sources to explain typical metamorphic fluxes. Introducing the assumptions that fluid expulsion keeps pace with metamorphic fluid production and that the duration of metamorphism is dictated by the heat conduction time scale ($\tau_{met} \sim l_c^2/\kappa$, where κ is thermal diffusivity, $O(10^{-6})$ m^2/s for crustal rocks), time-averaged fluxes are of the order

$$\bar{q} = \frac{w\rho_r \kappa}{\rho_f l_c} \sim O\left(10^{-12}\right)\mathrm{m/s}. \tag{14.19}$$

By introducing an additional assumption about the pressure gradient responsible for the average flux, Darcy's law can be inverted for time-averaged permeability (Ingebritsen and Manning 1999). The simplicity of this logic is seductive, but because metamorphic fluxes are dynamic such averages are misleading. For example, Fulton et al. (2009) reject the contention of Ague et al. (1998) that dehydration generated fluid overpressures may trigger faulting. The fallacy of the argumentation being that, by definition, the average permeability is the permeability necessary to accommodate metamorphic fluxes at lithostatic pressure, thus it is unsurprising that a dynamic metamorphic flux is inadequate to generate overpressures if this

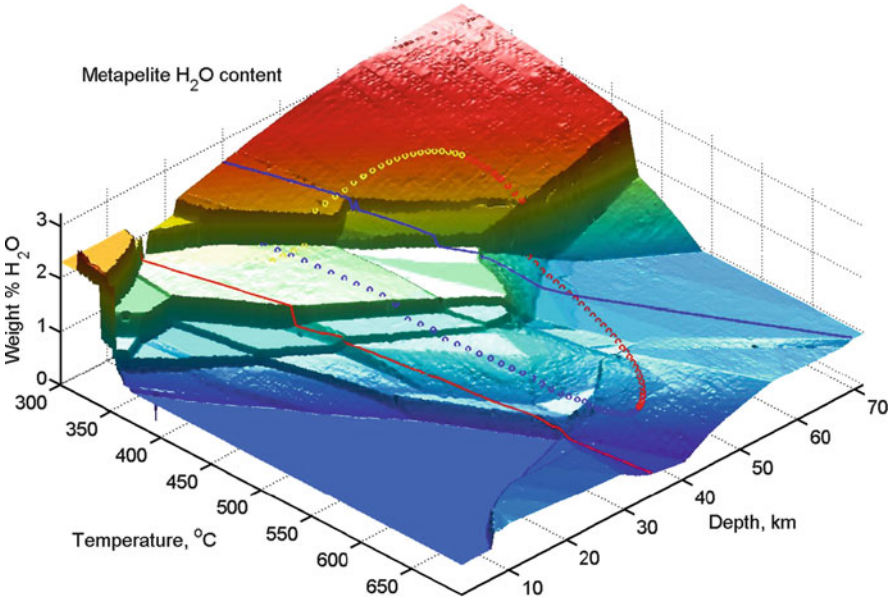

Fig. 14.3 Water-content for an average pelitic sediment composition (Plank and Langmuir 1998) as a function of temperature and pressure, computed assuming equilibrium with a pure H_2O fluid. Red and blue lines indicate hot (20°C/km) and cold (10°C/km) metamorphic geotherms. The increase in water-content at temperatures > 600°C is due to melting that occurs because the model assumes water-saturation. This melting does not occur if the water released by low temperature processes is expelled (Modified from Connolly 2010)

permeability is assumed as an initial condition. From the point of view of understanding dynamic flow, average permeability has no utility unless permeability is a static property. However, it would be fortuitous if this static permeability were exactly the permeability necessary to conduct metamorphic fluxes at lithostatic pressure. Thus, the pertinent issue to understanding lower crustal fluid flow is not the average permeability of the lower crust, but rather the background permeability that characterizes the environment prior to the onset of the flow perturbation of interest.

To illustrate the variability of metamorphic fluid production, consider equilibrium dehydration of a pelitic rock (Fig. 14.3). In the closed system limit, the classical lithostatic fluid pressure model requires that volume changes associated with devolatilization must be instantaneous. In the context of this model, the instantaneous dilational strain is a function of pressure and temperature and can be decomposed into components representing fluid and solid volumetric production rates (Fig. 14.4). The rates are broadly consistent with the expectation that metamorphic devolatilization is associated with a reduction in solid volume, but an increase in total volume; a behavior that would increase fluid pressure and drive dilational deformation in real systems. If hydrofracture provides an instantaneous dilational mechanism then the equilibrium model can be realized for the general case. Exceptions to this generality occur at the extremes of the metamorphic

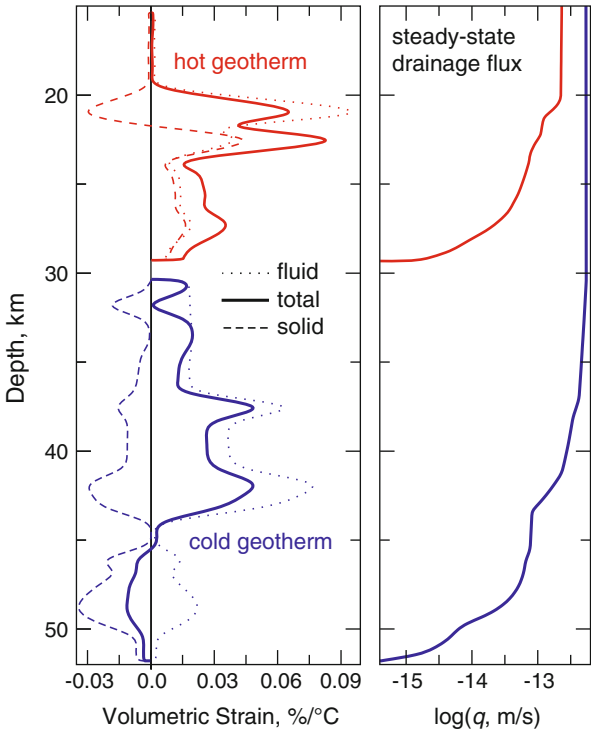

Fig. 14.4 Dehydration induced, isobaric strain, and steady-state fluid fluxes as a function of depth for the metamorphic model depicted in Fig. 14.3. The strain is resolved into the components due to fluid and solid production and corrected for the effect of thermal expansivity. Fluid and solid production rates are the product of the corresponding component of the isobaric strain multiplied by the metamorphic heating rate. The steady-state drainage flux q is the vertically integrated fluid production rate computed for a heating rate of 3°C/My. This is the flux required for drainage to balance fluid production. For the hot geotherm, the curves are terminated at the onset of melting because the melting process is dependent on the dynamics of fluid expulsion (Modified from Connolly 2010)

spectrum, i.e., at low temperature and high pressure or high temperature and low pressure. In the former case, the net volume change may be negative, an effect that would generate sub-lithostatic fluid pressures and therefore cause reaction rates to be limited by relatively slow viscous compaction mechanisms. In contrast, along high geothermal gradients the solid volume may increase (Fig. 14.4) during devolatilization requiring a more complex dilational deformation process than the hydrofracture mechanism assumed here.

Under the assumption that fluids are expelled upwards as rapidly as they are produced, metamorphic fluxes are the vertically integrated fluid production rate, i.e., the component of the dilational strain rate attributed to fluid generation. Taking a heating rate of 3 K/My and assuming consistent heat-conduction controlled metamorphism (England and Thompson 1984), fluid fluxes estimated in this way for both cool and warm geothermal conditions are comparable to the average flux deduced earlier (Fig. 14.4). However, the more detailed model illustrates that fluxes

must vary by orders of magnitude with depth. These fluxes place an upper bound on the effective permeability of the lower crust, because it would be impossible to generate elevated fluid pressure at a higher permeability. Unfortunately, there is little reason to expect that background permeabilities will be conveniently close to this upper bound, although they may well correlate with rates of metamorphism. This latter issue is topical because recent studies (Oliver et al. 2000; Dewey 2005; Ague and Baxter 2007; Warren et al. 2011) suggest that at least some episodes of regional metamorphism occur on time scales one to two orders of magnitude shorter than implied by the heat conduction time scale.

14.5 Fluid Flow in Compacting Media: Porosity Waves

Evidence that metamorphic devolatilization occurs at elevated fluid pressure leaves little doubt that devolatilization perturbs the pre-metamorphic hydrologic regime. In rigid rock, the dilational strain required for reaction progress is eliminated if the fluid is simultaneously drained by hydraulic diffusion. However, if the rocks initially contain fluid at or near lithostatic pressure, then, from Darcy's law, the fluid pressure gradient required for this drainage must be supralithostatic and is therefore inconsistent with the existence of lithostatic fluid pressure during metamorphism. If the definition of rigid is relaxed to allow for brittle failure at insignificant overpressure, the coupling between reaction rate and pressure is eliminated, but so too are the fluid overpressures that would be capable of explaining increased fluid drainage. Thus, without compaction, the effect of brittle failure is to generate a horizon of elevated porosity, filled by near lithostatically pressured fluid, sandwiched between relatively impermeable unreacted rocks. The horizon is analogous to a wet sponge in that it releases fluid only if it is squeezed. The weight of the overlying rocks acts as the agent for squeezing by, what has been argued here to be, predominantly, viscous compaction. The rate at which the fluid is drained is fundamentally limited by the permeability of the overlying rocks, but because these rocks are also deformable this permeability is dynamic. As noted earlier, the peculiar feature of fluid flow in this scenario is that it occurs in waves of fluid-filled porosity. An idealized 1-d, constant viscosity, model is employed here to explain why these waves form, after which the model is extended to account for more complex rheology and multidimensional effects.

14.5.1 Porosity Waves in Viscous Rock, Why?

For simplicity consider a constant volume devolatilization reaction that initiates at depth within an otherwise uniform rock subject to some small background fluid flux q_0 (Fig. 14.5). Initially, since the reaction is isochoric it does not perturb the background flux, but it does increase the porosity from ϕ_0 to ϕ_1 by reducing the solid volume. This porosity change increases the permeability within the reacted

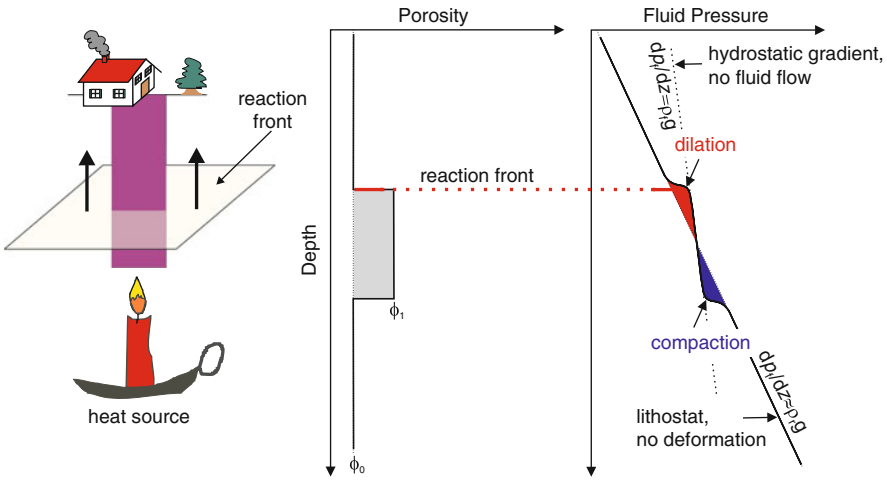

Fig. 14.5 Conceptual model of an isochoric metamorphic devolatilization reaction. The unreacted rock has porosity ϕ_0 and conducts the flux q_0. The reaction leaves a region of elevated porosity ϕ_1 in its wake. This high porosity region has a permeability $(\phi_1/\phi_0)^3$ times greater than in the unreacted rock (for $n_\phi = 3$ in Eq. 14.17). Because there are no dilational effects associated with an isochoric reaction, the flux in the permeable reacted region must initially be the same as the background flux. For this to be true Darcy's law requires that the effective pressure gradient in the reacted rocks must be $\Delta\rho g/(\phi_1/\phi_0)^3$; thus a factor of 2 increase in porosity reduces the fluid pressure gradient to within 12.5% of the hydrostatic gradient. As the vertical extent of the reacted rocks becomes larger with time, this condition causes finite effective pressure anomalies that lead to fluid expulsion. Non-isochoric reactions lead to a similar scenario, but with asymmetric pressure anomalies (Connolly 1997) (Modified from Connolly 2010)

rocks by a factor of $(\phi_1/\phi_0)^3$ (for $n_\phi = 3$ in Eq. 14.17). From Darcy's law, if fluid flux is constant then an increase in permeability must be compensated by a reduction in the fluid pressure gradient. Thus, an order of magnitude increase in permeability is sufficient to cause the fluid pressure gradient to relax to essentially hydrostatic values within the reacted rock. In turn, this relaxation gives rise to an effective pressure gradient such that pore fluids are overpressured above the center of the reacted zone and underpressured below it (Fig. 14.5). These pressure anomalies induce transient perturbations to the fluid flux above and below the reacted zone, but because the anomalies are antisymmetric there is no net drainage of fluid from the reacted layer as long as deformation is insignificant. However, the magnitude of the pressure anomalies must grow in proportion to the vertical extent of the reacted rocks with the result that deformation becomes inevitable. This deformation is manifest as compaction at the base of the reacted rocks and dilation at their top and has the effect of propagating the reaction-generated porosity upward (Fig. 14.6a). If the rate of propagation is high enough, then this mechanism can generate an isolated domain, or wave, of porosity that separates from the reaction front. Alternatively if the domain moves too slowly to detach from the source a wave train develops. The isolated wave and wave train correspond to steady-state solitary (Richter and McKenzie 1984; Barcilon and Richter 1986) and periodic (Sumita et al. 1996; Connolly and Podladchikov 1998) wave solutions of the

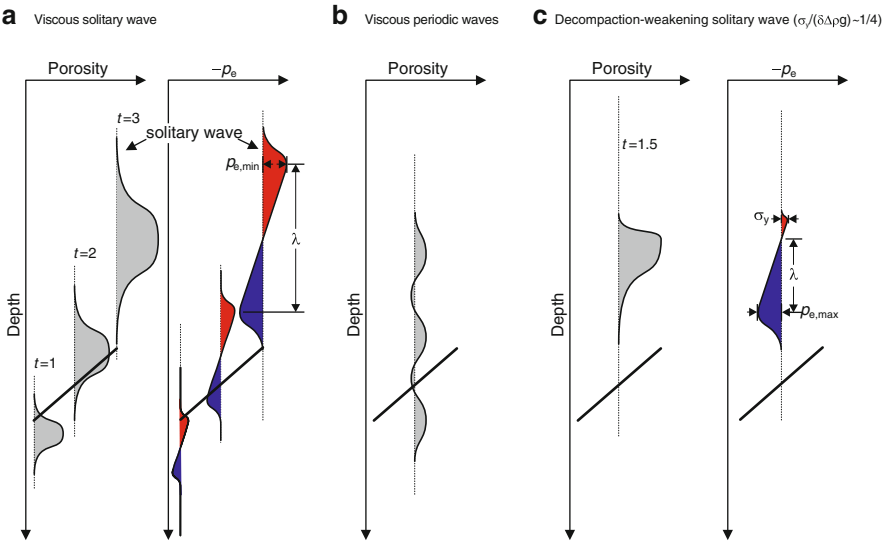

Fig. 14.6 Time evolution of reaction-generated porosity and fluid overpressure, $p_f - p$, profiles in a viscous solid matrix. For each profile the baseline is indicated by a vertical dotted line that corresponds to the background porosity, ϕ_0, or zero overpressure. In the symmetric viscous case (**a**), the magnitude of the fluid pressure anomalies within the reaction-generated porosity is proportional to the vertical extent of the high porosity. Thus, the anomalies grow as the reaction front advances upward until they become large enough to cause significant deformation. Thereafter, compaction at the base of the high porosity region squeezes fluid upward to the upper portion of the high porosity region where it is accommodated by dilational deformation. This process has the effect of propagating the reaction-generated porosity upward. The high porosity region detaches from the source when the compaction rate at the base becomes comparable to the fluid production rate giving rise to a solitary wave that propagates independently of its source (Richter and McKenzie 1984; Connolly 1997). For the solitary wave to be stable it must propagate with speed $v_\phi > n_\phi v_0$ (Appendix, Eq. 14.54). If the source is too weak to sustain a wave with this speed then a periodic wave train forms that is unable to separate from the source (**b**). These periodic waves dissipate if the source is exhausted. If the fluid overpressures are large enough to induce embrittlement, decompaction becomes viscoplastic (**c**), but the compaction remains viscous. In this case, the lower portion of the solitary wave is unchanged from the symmetric viscous case, but hydrofracturing acts as homeostat that regulates the overpressures in the *upper* portion of the wave. The scenarios depicted here assume that the speed at which the reaction front propagates upward is not much greater than the speed of fluid flow v_0 through the unperturbed matrix, in the alternative, fast devolatilization scenario (Sect. 14.5.3) waves detach from the source only after the cessation of devolatilization

equations that govern two-phase flow in an infinite viscous matrix (Fig. 14.6b and Appendix). In the case of the solitary wave solution, the steady state consists of a single isolated wave that propagates without dissipating. Because of its solitary character, this steady state can plausibly be realized in nature and has been verified in analog experiments (Scott et al. 1986). Additionally, numerical experiments have shown that solitary waves are resistant to perturbations, e.g., if two waves collide they regain their initial form after the collision (Richter and McKenzie 1984; Scott and Stevenson 1986). In contrast, the periodic steady state consists of an infinite

wave train, which cannot be realized in nature. Thus, although a finite periodic wave train, in close proximity to the infinite steady state, may develop in response to a fluid source, once the source is exhausted the finite wave train will spread and dissipate to smooth flow.

14.5.1.1 Why Don't Solitary Waves Dissipate?

It is natural to wonder why steady-state wave solutions exist at all. The origin of the phenomenon is the non-linear relation between porosity and permeability (e.g., Eq. 14.17) that permits flow perturbations to grow into shocks that propagate more rapidly than the fluid flows by hydraulic diffusion (Spiegelman 1993). This phenomenon is most easily explained for a matrix with no strength (i.e., the classical metamorphic model) in which case fluid pressure is lithostatic and fluid flux and velocity are solely a function of porosity. Consider then a situation in which a region with a large flux ($\mathbf{q}_1 = \mathbf{v}_1\phi_1$) is overlain by a region with a small flux ($\mathbf{q}_0 = \mathbf{v}_0\phi_0$) and that the regions are, initially, connected by a region in which the porosity decreases upward (Fig. 14.7a). From Eqs. 14.9 to 14.17, in terms of the fluid velocity in the low porosity region, the fluid velocity at any other porosity is

$$\mathbf{v} = \mathbf{v}_0(\phi/\phi_0)^{n_\phi - 1}. \tag{14.20}$$

At any point where the porosity gradient is finite and decreases in the direction of flow, the divergence of the flux (i.e., the difference between the flux into and out of an infinitesimal volume) is also finite. This divergence must be manifest by an increase in porosity, i.e., dilational strain, which leads to a steepening of the porosity gradient and, ultimately, the formation of a porosity shock (i.e., a self-propagating step in the porosity profile, Fig. 14.7b). Because the shock is moving more rapidly than the fluid in front of shock, in a reference frame that moves with the shock, the flux from the unperturbed matrix must be directed toward the shock. Consequently, as the shock propagates it gains fluid volume at the rate $q_1 - q_0$ from the low porosity region. As the porosity behind the shock is constant, conservation of the fluid volume requires that the shock velocity satisfies

$$\mathbf{v}_\phi = (\mathbf{q}_1 - \mathbf{q}_0)/(\phi_1 - \phi_0), \tag{14.21}$$

or, making use of Eq. 14.20,

$$\mathbf{v}_\phi = \mathbf{v}_0(1 - (\phi_0/\phi_1)^{n_\phi})/(\phi_1/\phi_0 - 1). \tag{14.22}$$

From Eq. 14.22, the smallest discrepancy between the velocity of the shock, and that of the fluid behind the shock, occurs in the limit that the shock is small, i.e., $\phi_1 \to \phi_0$. The solitary porosity wave represents a steady state in which the finite strength of the matrix balances the tendency of fluid flow to steepen the porosity profile. Although the solitary wave is more complex than the simple shock, the

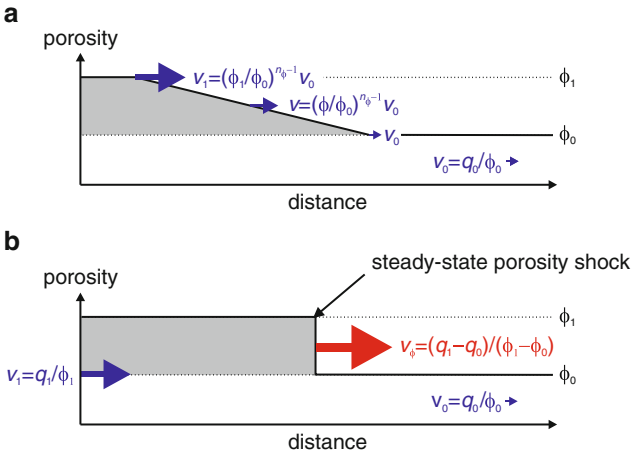

Fig. 14.7 Formation of a porosity shock during fluid flow through an inviscid matrix (i.e., the classical metamorphic model). If the matrix is inviscid, then fluid pressure must be lithostatic and fluid velocity is solely a function of porosity. Consequently, if porosity decreases in the direction of flow, fluid in the high porosity direction catches up to the fluid in the low porosity region. This process increases the porosity gradient until it becomes infinite. At which point, the resulting step in the porosity profile corresponds to a porosity shock. In a reference frame that moves with the shock, the fluid flux from the unperturbed matrix is negative; thus the shock must travel more rapidly than the fluid behind it (Eq. 14.22). The minimum discrepancy between the fluid and shock velocities occurs when the porosity behind the shock is only infinitesimally larger than the background value. In this case, the velocity of the shock is $n_\phi v_0$, and corresponds to the minimum velocity at which the solitary wave solution is stable in a matrix with a finite viscosity (Appendix, Eq. 14.54)

solitary wave must have the same properties as the simple shock at the conditions where it connects to the unperturbed porosity. At this point the fluid velocity is $\mathbf{v}_0$ and, from Eq. 14.22, the velocity of the simple shock is $n_\phi \mathbf{v}_0$. Thus, a requirement for the existence of steady-state solitary porosity waves is that they move ~ n_ϕ times faster than the flow through the unperturbed matrix (Appendix, Eq. 14.54). As in the simple shock, the solitary wave catches up with fluid flow through the background porosity with the consequence that a geochemical signal from the wave source may become diluted with time. The magnitude of this effect can be quantified (Spiegelman and Elliott 1993), but it is insignificant for large amplitude waves, i.e., $\phi_{max} >> \phi_0$.

14.5.2 One-Dimensional Isothermal Waves: How Big, How Fast, and How Much?

In the limit of a small perturbation to steady fluid flow through a uniform fluid-filled porosity, compaction phenomena develop on a natural length scale known as the viscous compaction length (McKenzie 1984). For a power-law viscous matrix this scale (Appendix, Eq. 14.63) is

$$\delta = \phi_0^{\frac{n_\phi - 1}{n_\sigma + 1}} \sqrt[n_\sigma + 1]{\left(\frac{2}{n_\sigma + 1}\right)^{n_\sigma} \frac{c_\phi}{c_\sigma A \mu (\Delta\rho g)^{n_\sigma - 1}}}, \tag{14.23}$$

The compaction length is an estimate of the depth interval over which the matrix can sustain a non-lithostatic pressure gradient and, as such, it is unsurprising that it increases both with the strength ($\propto 1/A$, Eq. 14.16) of the matrix and the ease with which fluid flows through it ($\propto c_\phi/\mu$). The speed of fluid flow at lithostatic fluid pressure through the unperturbed matrix, $v_0 \approx c_\phi \phi_0^{n_\phi - 1} \Delta\rho g/\mu$ (Eqs. 14.4 and 14.9), provides a natural scale for the speed of compaction processes. From this speed the compaction time scale (δ/v_0) is

$$\tau = \phi_0^{\frac{n_\sigma(1 - n_\phi)}{n_\sigma + 1}} \sqrt[n_\sigma + 1]{\left(\frac{\mu}{c_\phi (\Delta\rho g)^2}\right)^{n_\sigma} \Big/ A}, \tag{14.24}$$

The compaction scales given by Eqs. 14.23 and 14.24 separate the porosity ϕ_0 of the fluid-rock aggregate from material properties (A, $\Delta\rho$, μ, c_ϕ) that are, at least in principle, measurable quantities. In metamorphic problems this porosity is an unknown property of the initial state. The challenge presented by metamorphic fluid expulsion is to find observations that constrain the compaction scales and thereby this initial state. Because the compaction scales are formulated in terms of the initial state they represent, for $n_\sigma > 1$ and $n_\phi > 1$, a lower bound on the length scale and an upper bound on the time scale for fluid expulsion.

Given the uncertainties in the material properties involved in the compaction scales, it may be preferable to use observational constraints to infer the magnitudes of these scales. To this end, background flux q_0, which is presumably less than the time-averaged metamorphic flux, provides a useful proxy for the hydraulic material properties. Taking the observations of Young and Rumble (1993), van Haren et al. (1996), and Graham et al. (1998) to be indicative of compaction time scales O(10^4) y at amphibolite facies conditions ($T = 773 - 923$ K), in conjunction with a plausible estimate for $v_0 = q_0/\phi_0$ of 10^{-10} m/s, the compaction length ($\delta = \tau v_0$) consistent with these observations is 31 m. Clearly, it would be preferable to have direct observational constraints on the compaction length scale, as might be provided by variation in the pressures ($O(2\delta\Delta\rho g)$) recorded by syn-metamorphic fluid inclusions or, as discussed subsequently, by the length scale ($O(\delta)$) for lateral fluid flow. However, taken at face value, an $O(10^4)$ y time scale and an $O(10^2)$ m length scale implies a viscous rheology roughly three orders of magnitude weaker than given by Eq. 14.14 for tectonic strain rates $O(10^{-15})$ s^{-1}. A discrepancy of this magnitude can be explained if fluid expulsion is contemporaneous with pulses of intense tectonic deformation that lower the effective viscosity of the crust; an explanation consistent with a non-uniformitarian model of deformation and metamorphism (Oliver et al. 2000; Dewey 2005; Ague and Baxter 2007).

There is no fundamental principle that dictates a steady-state balance between metamorphic fluid production and transport, but for the range of conditions

investigated by numerical simulations of metamorphic compaction-driven fluid flow (Connolly 1997; Connolly 2010) such a balance does develop locally. A requirement for this balance is that the time-averaged flux associated with the passage of a wave must be greater than or equal to the vertically integrated production, $\bar{q}$, because a wave with $q_e < \bar{q}$ would be unable to separate from its source. This time-averaged flux is

$$q_e = \frac{v_\phi}{\lambda} V_e^{1d} \tag{14.25}$$

where λ and v_ϕ are the length and speed of the wave, and

$$V_e^{1d} = \int_{-\lambda/2}^{\lambda/2} (\phi - \phi_0) dz \tag{14.26}$$

is the fluid volume associated with the wave, which in one dimension has units of length. If $q_e > \bar{q}$, then the waves must be separated by a depth interval of

$$\Delta z = \lambda(q_e/\bar{q} - 1)$$

In 1-d numerical simulations, the transient dynamics of wave separation are such that $q_e/\bar{q}$ is typically < 2 (Connolly 1997). This result suggests that, to a first approximation, the properties of waves expected in metamorphic environments can be predicted from the steady-state solitary wave solution to the compaction equations (Fig. 14.8). The solitary wave solution does not exist for values of $q_e/q_0 < 2$ (Appendix, Eq. 14.53), thus weak sources, or strong background fluxes, will generate periodic waves that degenerate to uniform flow once the source is exhausted. Periodic solutions to the compaction equations exist for all conditions; however numerical (Richter and McKenzie 1984; Scott and Stevenson 1986; Wiggins and Spiegelman 1995; Connolly 1997) and analog (Scott et al. 1986) simulations suggest that the solitary wave solution is the stable solution whenever it is a possible solution. The reason for this stability is unclear, but is most probably related to the fact that the solitary wave is the more effective expulsion mechanism and therefore maximizes the rate of dissipation of gravitational potential energy.

Because the matrix recovers to the background porosity asymptotically in a steady-state solitary wave (for $n_\sigma \geq 1$), the wavelength of the true steady state is infinite (Appendix, Eq. 14.59). For practical purposes, it is desirable to define an effective wavelength, which defines the extent of the wave that includes the bulk of the anomalous porosity. Two non-arbitrary measures of wavelength are the distance between the points of minimum and maximum effective pressure (λ) and twice the second moment of the porosity distribution within the wave (λ_1, Fig. 14.8c), the former value being roughly half the latter. Comparison of the excess volume obtained by integrating the porosity over these intervals to the total excess volume obtained by integrating over infinite space (dashed curve, Fig. 14.8d) shows that,

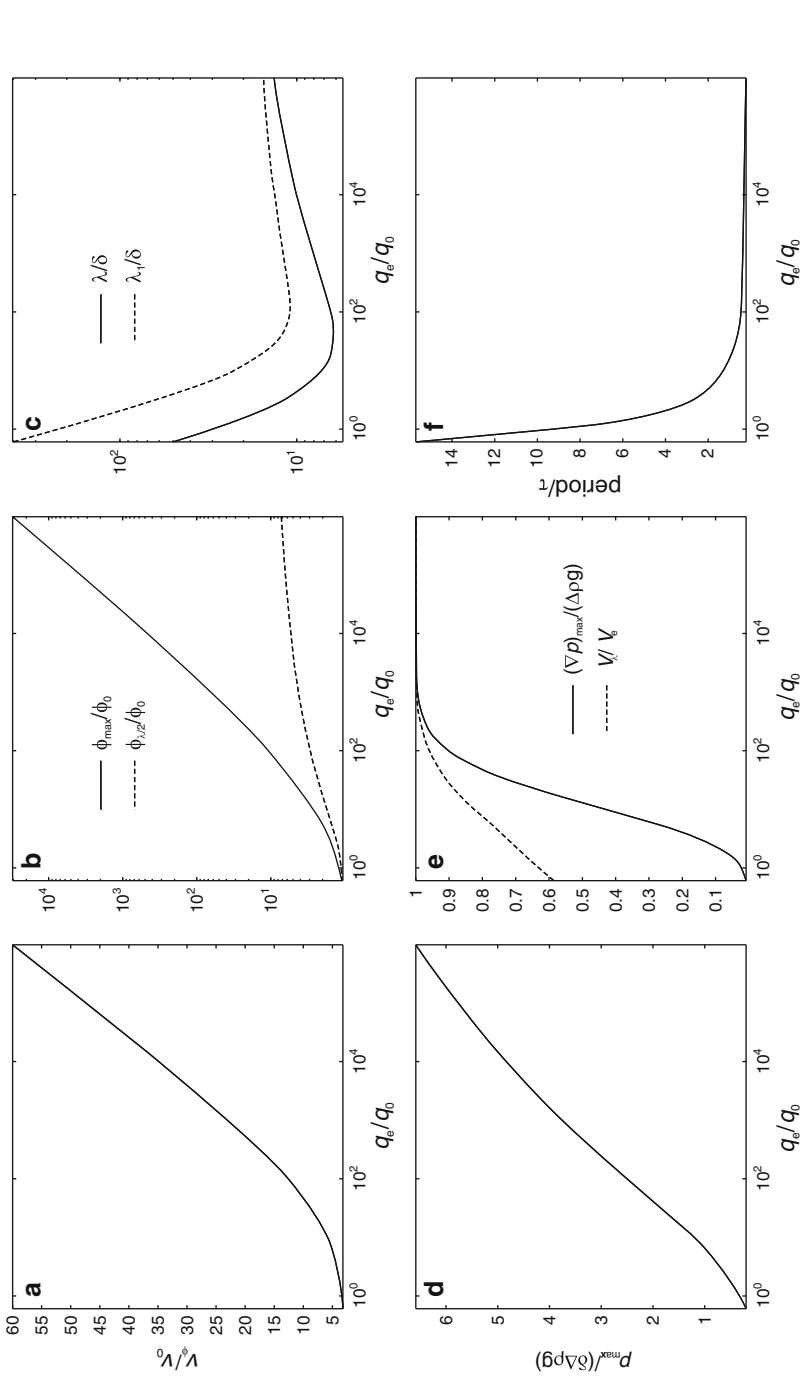

Fig. 14.8 Steady-state 1-d solitary wave properties (for $n_\sigma = n_\phi = 3$) as a function of the excess fluid flux q_e, which is the time-averaged flux associated with the passage of a porosity wave estimated as the product of the wave period and its excess volume. The power law exponent does not influence the speed-amplitude relation, but wavelength increases inversely with n_σ. (**a**) Wave speed, v_ϕ. (**b**) Maximum porosity ϕ_{max}, and porosity at the depth of maximum effective pressure within a wave (Fig. 14.6a). (**c**) Two measures of the spatial extent of solitary waves: λ is the depth interval between the minimum and maximum effective pressure (Fig. 14.6a), and λ_1 is the second moment of the porosity distribution. (**d**) Maximum effective pressure within the wave. (**e**) Maximum effective pressure gradient ($\phi = \phi_{max}$, $p_e = 0$) and the fraction of the total excess volume of the wave that occurs within the depth interval $\pm\,\lambda/2$ around ϕ_{max}. (**f**) Wave period, λ/v_ϕ

even at the minimum q_e for solitary wave stability, >80% of the porosity of a wave occurs within a distance of $\pm\ \lambda/2$ from its center. Accordingly, λ is adopted here as the measure of wavelength rather than the more conservative measure λ_1. The solitary wave period, λ/v_ϕ, is the time required for a wave to travel its wavelength.

To illustrate the quantitative implications of the solitary wave solution, consider the initial condition $\phi_0 = 10^{-4}$, $q_0 = 10^{-14}$ m/s, $\tau = 10$ ky, and $\delta = 31$ m, which, as discussed previously, is chosen to be consistent with the timing of fluid-rock interaction during amphibolite facies metamorphism (Young and Rumble 1993; van Haren et al. 1996; and Graham et al. 1998). From this condition, and the properties of the solitary wave steady state (Fig. 14.8), the waves required to conduct a typical metamorphic flux $\bar{q} = 10^{-12}$ m/s (i.e., $q_e/q_0 = \bar{q}/q_0 = 10^2$) have $\lambda = 200$ m, $\phi_{max} = 1.0{\cdot}10^{-3}$, travel at $v_\phi = 39$ m/ky, and are associated with fluid pressure anomalies of 1.4 MPa. These pressure anomalies are small enough that a viscous dilational mechanism for wave propagation is plausible. The sensitivity of this result is demonstrated by considering the effect increasing $\bar{q}$ to 10^{-10} m/s, which is consistent with the rate for Dalradian regional metamorphism inferred by Ague and Baxter (2007). For this increased flux, $\lambda = 320$ m, $\phi_{max} = 55{\cdot}10^{-3}$, $v_\phi = 110$ m/ky, and $p_{max} = 2.9$ MPa; the most prominent difference being the large increase in porosity.

14.5.3 *Fast Versus Slow Devolatilization and Complex Fluid Sources*

The knife-edge sharp, constant volume, devolatilization reaction used so far for purposes of illustration may seem unrealistic, but it captures the essence of the fluid expulsion problem, which is not how fluid is released, but rather how it escapes. The key to predicting the waves that are likely to evolve in response to more complex devolatilization processes is to obtain plausible estimates for both the background flux that the system is capable of accommodating without appreciable dilational deformation and the excess flux generated by devolatilization that must be accommodated by porosity waves.

The relationships between porosity wave speed and excess flux (Fig. 14.8a) and between excess flux and wave amplitude (Fig. 14.8b) indicate that extraordinarily large porosities are required to generate waves that travel more than two orders of magnitude faster than the speed of the fluid flow in the unperturbed matrix. As the analytical formulation ignores large porosity effects that lead to a further weakening of the dependence of speed on amplitude, it is reasonable to conclude that if natural porosity waves exist, then they do not propagate at speeds $>> v_0$. Given that a porosity wave can only escape from a devolatilization reaction front if it travels faster than the front, these considerations imply that the wave nucleation scenario outlined in Sect. 14.5.1 represents the limiting case of slow devolatilization, wherein the devolatilization front propagates at speeds that are comparable

to or less than v_0. In the alternative fast devolatilization scenario, devolatilization generates a high porosity source region. Porosity waves cannot escape from this source until lithological heterogeneity or geodynamic factors hinder the advance of the devolatilization front. If it is assumed that the material properties of the reacted and unreacted rocks do not differ significantly, then the porosity increase within the source region decreases the time scale for intra-source fluid expulsion (Eq. 14.24). This increase in efficiency has the consequence that the excess flux delivered to the upper boundary of the source region is independent of the processes in the unreacted rocks, which compact on a longer time scale. If the porosity, ϕ_1, within the source is $>> \phi_0$, then this excess flux is $\sim q_0(\phi_1/\phi_0)^{n_\phi}$ and the waves that ultimately evolve from the source can be expected to carry a flux that is greater than, but comparable to this flux. Spiegelman (1993) demonstrated that in the waves which nucleate at the boundary between the source and unreacted rocks are not true solitary waves. However, for large porosity contrasts, i.e., $\phi_1 >> \phi_0$, the distinction is not important and is diminished still further in models that account for the elastic compressibility of the fluid (Connolly and Podladchikov 1998).

The dehydration model presented earlier suggests that in nature devolatilization may occur by many reactions simultaneously over a depth interval of several kilometers (Fig. 14.3). The increase in porosity caused by these reactions increases the compaction length within such an interval, an effect that will tend to blur the influence of individual reactions. Thus the characteristics of waves that would evolve above such an interval can be anticipated by equating the excess flux to either the vertically integrated fluid production in the slow devolatilization limit, or to $q_0(\phi_1/\phi_0)^{n_\phi}$ in the fast limit.

A reaction with a finite isobaric volume change leads to a coupling between devolatilization kinetics, temperature, and fluid pressure, but this coupling does not hinder the evolution of porosity waves (Connolly 1997). Finite volume change reactions also influence the initial pressure distribution, but regardless of this distribution, deformation will cause the system to evolve toward a state in which effective pressures are low or negative at the top of the reacted region. For example, a reaction with a positive (isobaric) volume change may initially generate fluid overpressure throughout the reacted rocks, with the result that hydraulic diffusion drives fluid both upward and downward from the reaction front. Thus the flux within the reacted rocks is not constrained by symmetry. However, provided the permeability within the reacted rocks is much higher than in the surroundings, the fluid pressure gradient will approach the hydrostatic value. Thus, the greatest overpressures will occur at the top of the reacted column. This distribution must lead to higher rates of dilational deformation at the top of the column and, ultimately, underpressured porosity at depth.

Despite the complexities that may influence the kinetics of individual devolatilization reactions, there is reason to believe that overall rates of metamorphic devolatilization do not differ greatly from those predicted by equilibrium models. Specifically, if rocks cannot sustain large fluid overpressures then the thermal overstepping of the equilibrium conditions is likely to be the primary manifestation of disequilibrium. As reaction kinetics are typically an exponential function of

temperature (Rubie and Thompson 1985), moderate thermal overstepping should accelerate kinetics to the point at which they become limited by the rate of energy input as would be the case for an equilibrium system. This logic assumes that rocks cannot support large elastic stresses. That this assumption is not a universal truth has been demonstrated in experiments on reactive systems in which a fluid inclusion achieves a non-hydrostatic equilibrium with its surroundings (Kerschhofer et al. 1998; Mosenfelder et al. 2000; Milke et al. 2009). Vrijmoed et al. (2009) argue that strength contrasts in rocks are capable of generating large scale fluid inclusions that sustain pressures far above the lithostatic load. An effect of this nature has been invoked to explain the seemingly metastable persistence of volatile-bearing rocks (Padron-Navarta et al. 2011).

14.5.4 Multidimensional Viscous Porosity Waves

The 3-d expression of the 1-d porosity wave just discussed corresponds to a sill-like structure (Fig. 14.9b). However in two and three dimensions both numerical (Scott and Stevenson 1986; Stevenson 1989; Wiggins and Spiegelman 1995) and analytical (Barcilon and Lovera 1989) models show that 1-d solitary waves are unstable with respect to circular and spherical solitary waves. This instability is demonstrated numerically for fluid flow from a high porosity region, an analogy for a metamorphic fluid source, by introducing random noise into the initial porosity distribution (Fig. 14.9a). Although the 2-d waves (Fig. 14.9c) appear significantly different from the 1-d waves (Fig. 14.9b) that evolve from the initial porosity distribution without noise, it emerges that their properties are well approximated by applying radial symmetry to the porosity distribution of the 1-d solitary wave solution (Connolly and Podladchikov 2007). Thus, 1-d and 2-d solitary waves have an essentially equivalent relation between amplitude and speed. Although untested, it is assumed that the same approximation can be made in 3-d by applying spherical symmetry to the 1-d porosity distribution. That the 2-d approximation is nearly exact in the limit that the maximum porosity is $> 10\ \phi_0$ is verified by comparing the relationship between wave velocity and amplitude in analytic (Fig. 14.8) and numerical results (Fig. 14.9). The reason for the increased speed of 2-d waves compared to 1-d waves emanating from a comparable source is primarily the effect of a weak spatial focusing of the source flux in the 2-d case. The most important distinction between planar and circular waves is the existence of strong lateral pressure gradients associated with the dipolar pressure field of circular waves (Figs. 14.9d and 14.10a). Thus, in contrast to the unidirectional fluid flow of planar waves, fluid flow in circular waves is characterized by a circular pattern in which lateral fluxes are of comparable magnitude (Scott 1988; Connolly 2010). The circular pattern develops in the reference frame of the wave (Fig. 14.10a), but, in the reference frame of the solid matrix, passage of a wave is marked first by fluxes with a lateral component away from the vertical axis of the wave, followed by a period in which the lateral component is directed toward the axis. During this oscillation, the vertical component of the flux is always upward.

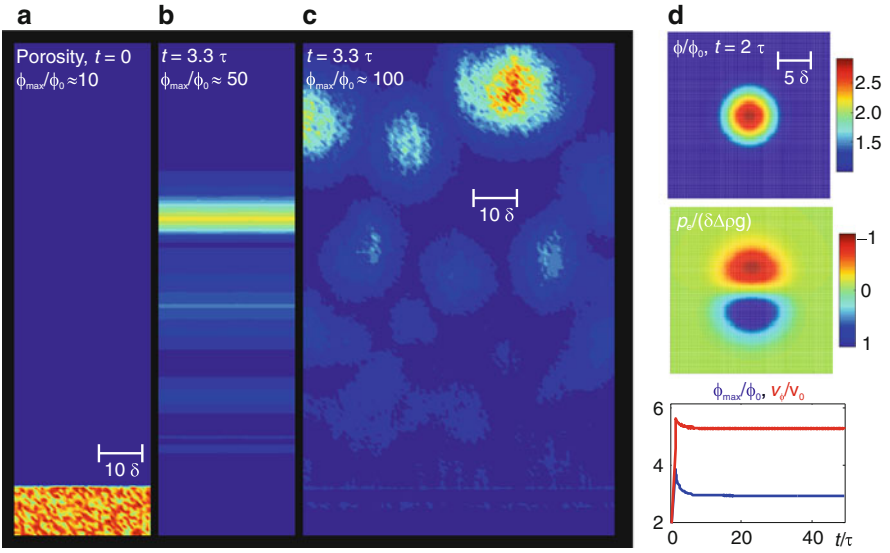

Fig. 14.9 Two-dimensional numerical simulations of porosity waves initiating from high porosity horizons that differ only in that in one case random noise is added to the initial porosity distribution. The simulations are for a Newtonian matrix ($n_\sigma = 1$, $n_\phi = 3$). If the initial porosity is perfectly smooth, 1-d sill-like waves nucleate from the source (**b**). However, if white noise is added to the initial porosity distribution as depicted in (**a**), the 1-d waves become unstable with respect to circular 2-d waves (**c**). The 2-d waves cause spatial focusing of the source flux. Consequently the 2-d waves have larger amplitudes and higher velocities than 1-d waves initiating from a similar source. Numerical simulations have also shown that the stable viscous solitary wave geometry in 3-d is spherical (Wiggins and Spiegelman 1995). (**d**) A numerical simulation of a 2-d wave nucleated from a small circular source region, illustrating the dipolar effective pressure field and the short duration of transient effects (i.e., the wave has essentially reached a steady state by $t/\tau \sim 2$). Wave properties along the vertical axis of 2-d waves, with $\phi_{max}/\phi_0 > 10$, are indistinguishable from those predicted for 1-d waves with the same amplitude (Connolly and Podladchikov 2007)

14.5.5 Porosity Waves in an Upward Strengthening Crust

The preceding discussion has ignored the temperature dependence of the viscous rheology, which is responsible for the upward strengthening of the lower crust. From Eq. 14.12, the compaction length and time scales increase exponentially with decreasing temperature towards the Earth's surface, increasing by a factor of $(n_\sigma + 1)^{-1}$, for a decrease in depth comparable to the viscous e-fold length l_A (Eq. 14.15, Fig. 14.1). This effect makes achievement of true steady-state waves a mathematical impossibility because the compaction scales vary between the top and bottom of a wave (Connolly 1997). The strength of this variation can be assessed by comparing the steady-state wavelength λ to l_A. If $\lambda << l_A$, then the rheological variation within the wave is weak and a quasi-steady state may arise such that at any point in time the properties of the wave closely approximate the

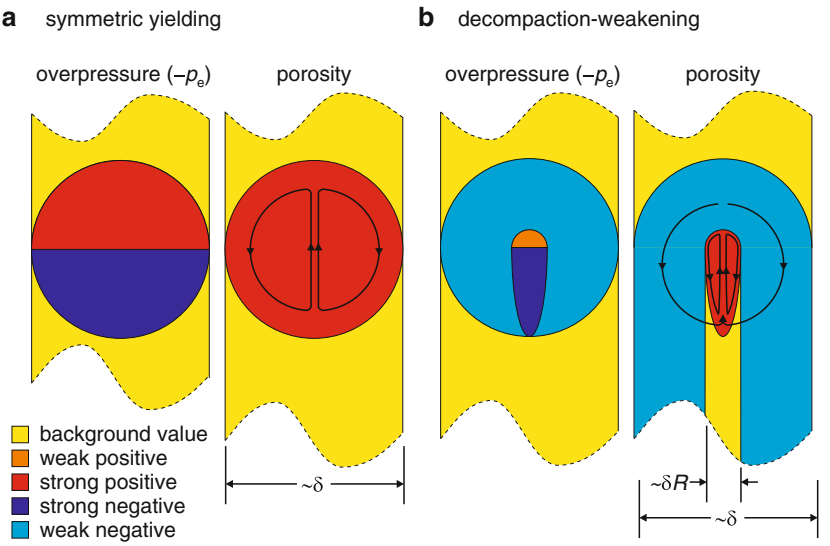

Fig. 14.10 Illustration of the scaling arguments used to relate the solitary wave solution in the symmetric viscous case (**a**) to the solitary waves that develop in a matrix with decompaction weakening (**b**). *Colors* indicate regions of the matrix that are characterized by weakly and strongly depressed or elevated values of overpressure and porosity. Approximate fluid flow paths, relative to a reference frame that moves with the porosity wave, are shown in the porosity map. The true paths do not close because the wave is subject to a small fluid flux from the background porosity (Fig. 14.7). This discrepancy is insignificant in large amplitude waves. In the reference frame of the solid, the vertical component of compaction driven fluxes is upward. In the symmetric case, the pressure distribution associated with a porosity wave is an antisymmetric dipole that induces balanced fluid circulation so the wave has no tendency to gain or lose mass (Fig. 14.11d). With decompaction weakening, fluid underpressures and compaction develop on the length scale δ as in the symmetric viscous case, whereas decompaction and overpressure develop on the shorter length scale δR. Thus, decompaction generates an elevated region of porosity and pressure analogous to the *upper* hemisphere of the symmetric viscous case, but on this shorter length scale. Restoration of this elevated porosity occurs on the length scale δ, which causes the compacting portion of the wave to develop a semi-ellipsoidal geometry. Fluid underpressure in the compacting region relaxes on the length scale δ causing compaction of the matrix in advance of the wave as well as in laterally adjacent portions of the matrix that have not been perturbed by decompaction. The asymmetric pressure distribution causes unbalanced fluid circulation, with the result that the wave gains mass from the matrix as it propagates, this imbalance is indicated schematically by the outermost, unclosed, flow path

steady state. In this regime, waves slow and spread as they propagate upward. In the limit $\lambda \rightarrow l_A$ this quasi-steady state becomes infeasible because compaction within a wave occurs much more rapidly than decompaction. At this point, the local compaction length scale becomes meaningless for compaction processes in the vertical direction, and l_A determines the vertical length scale (Connolly and Podladchikov 1998). In the absence of strong lateral thermal gradients, as assumed here, the local compaction length dictates the scale of lateral processes, thus,

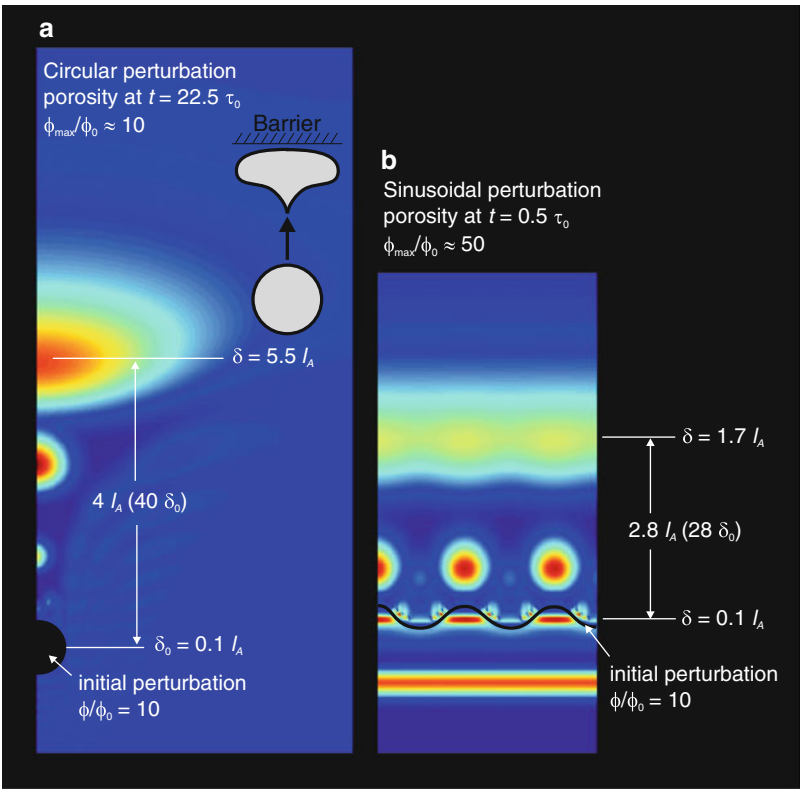

Fig. 14.11 Two-dimensional numerical simulations of viscous porosity waves in a rock matrix that strengthens upward due to thermal activation on the length scale l_A (Fig. 14.1). This effect causes the local compaction length δ to increase upward from its initial value δ_0; the simulations are for Newtonian rheology ($n_\sigma = n_\phi = 3$). (**a**) If the source is at depth such that $\delta_0 < l_A$, the quasi-steady state waves mimic the circular viscous steady-state, but spread as they rise upward until their wavelength approaches l_A at which point the waves flatten to oblate ellipsoids with vertical length scale l_A and horizontal length scale δ. The wave velocities decay exponentially upward on the length scale l_A. (**b**) Waves are generated from a high porosity layer with a sinusoidal upper boundary at depth such that $\delta_0 < l_A$. This simulation demonstrates that the effect of thermal activation is to restabilize 1-d solitary waves when wavelength approaches l_A (Modified from Connolly and Podladchikov (1998))

thermal activation gives rise to an intrinsic anisotropy to compaction-driven fluid flow.

The consequences of thermal activation for the 2- and 3-d viscous solitary wave solutions is demonstrated by a numerical experiment in which upward propagating waves are induced from a circular source (Fig. 14.11a) . At the initial depth, the waves are small in comparison to l_A and approximate the circular 2-d steady state. As the waves migrate upward their wavelength becomes comparable to l_A and they flatten to ellipsoidal structures with the horizontal length scale controlled by the local value of δ and the vertical length scale limited by l_A. A second numerical

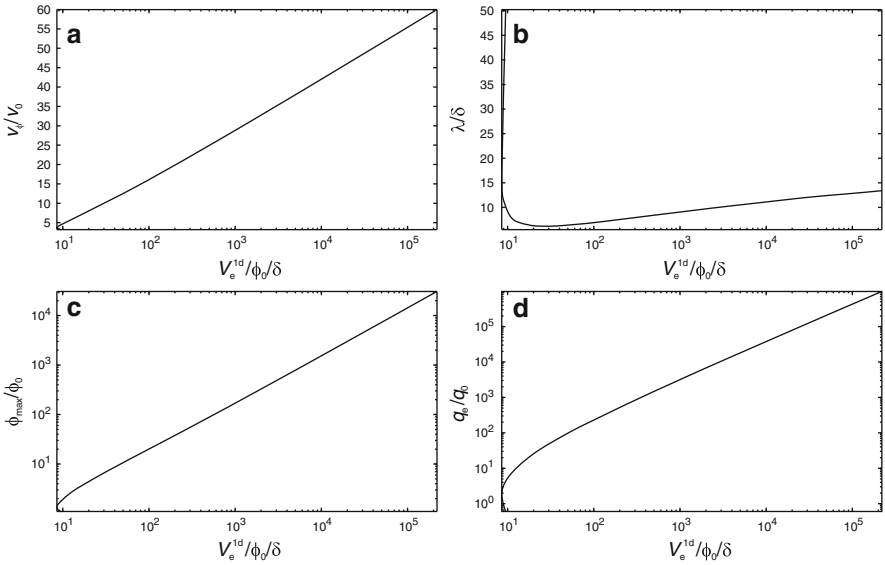

Fig. 14.12 Steady-state 1-d solitary wave properties in a power law ($n_\sigma = n_\phi = 3$) viscous matrix as a function of the excess volume (V_e^{1d}, Eq. 14.26). These properties can be used to predict quasi-steady state wave evolution in upward strengthening rocks as a function of the local compaction length. See text for discussion

experiment, in which waves initiating from a horizontal source are destabilized by a perturbation, shows that the effect of thermal activation is to restabilize 1-d planar waves (Fig. 14.11b). To show that this process is relevant to crustal fluid flow it is necessary to show that the wavelength of quasi-steady state waves will approach the l_A at the brittle-ductile transition (Fig. 14.1). This cannot be established from wave properties expressed as a function of excess flux because this flux decays as waves slow. However, quasi-steady state waves may conserve the excess fluid volume

$$V_e = \int\int\int (\phi - \phi_0) \mathrm{d}x\mathrm{d}y\mathrm{d}z \tag{14.27}$$

and therefore wave evolution can be predicted as a function of V_e (Fig. 14.12) provided $\lambda < l_A$. There are two complications in such predictions. The more difficult is that if waves evolve from 3-d structures, it is necessary to account for lateral variations in porosity. To avoid this complexity, the waves are approximated here as 1-dimensional. This approximation has the consequence that waves lengthen more rapidly than they would if 3-d geometry were taken into consideration. The second complication is that the dimensionless excess volume has a minimum at $V_e^{1d}/\delta/\phi_0 \sim 8$ (Fig 14.13a), thus a wave that initiates with $V_e^{1d}/\delta/\phi_0 > 8$ and broadens upward due to thermal activation cannot increase its wavelength above $\lambda_{max} \sim 17\ \delta$, the wavelength at $V_e^{1d}/\delta/\phi_0 \sim 8$, and must decay to the dissipative periodic solution as it propagates above this point, i.e., at $v_\phi \approx 3.5\, v_0$, slightly above the minimum velocity at which the solitary solution is stable. Returning to the

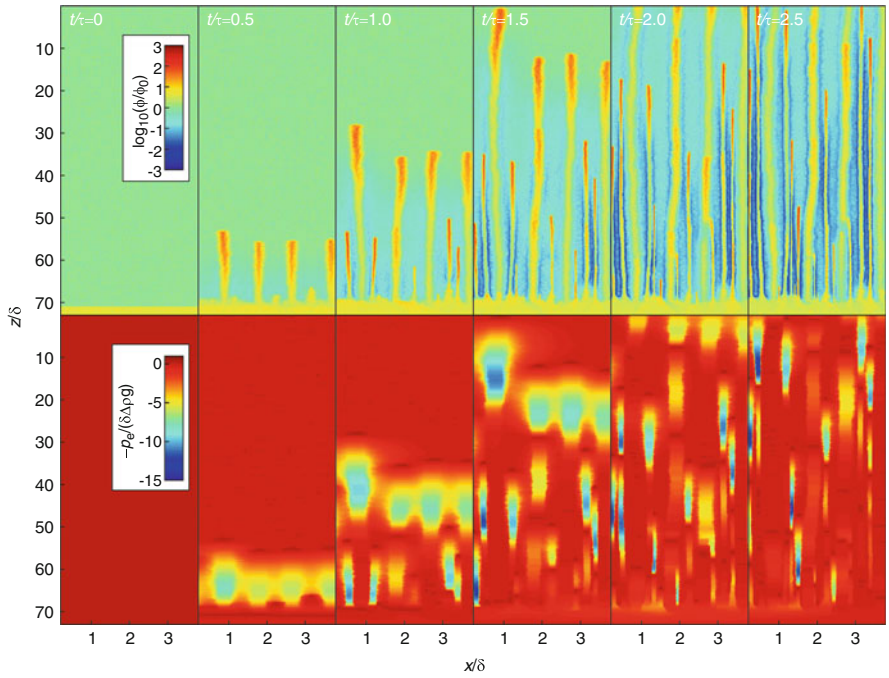

Fig. 14.13 Two-dimensional numerical simulation of fluid flow through a matrix with decompaction weakening ($R = 0.03$) as it evolves from a layer with elevated porosity of thickness 60 δ that is bounded from above and below by regions with an order of magnitude lower porosity. *Upper panels* show porosity in the uppermost portion of the layer and in the overlying region. *Lower panels* show the corresponding distribution of fluid overpressure. Initial waves ($t = \tau/2$) form with characteristic spacing identical to the viscous compaction length and leave a trail of slightly elevated porosity, flanked by a fluid depleted matrix. Depletion of the matrix reduces the local compaction length scale for the initiation of subsequent waves ($t = \tau$). These waves collect within the trails of the initial waves, so that at 30 –40 δ from the initial obstruction, flow is again channelized on the length scale δ. By analogy with the 3-d viscous case (Wiggins and Spiegelman 1995), it is presumed that the 3-d expression of the channels would be pipe-like structures. However, in the presence of far field stress, kinematic effects would flatten the tubes in the direction of the minimum horizontal stress (Modified from Connolly and Podladchikov (2007))

amphibolite-facies example (Sect. 14.5.2), if thermal activation is the sole source of variability in the compaction scales, then from Eqs. 14.12, 14.23, and, 14.24 then the compaction scales can be expressed as a function of temperature by

$$\delta = \delta_0 \exp\left[\frac{Q}{n_\sigma + 1}\frac{T_0 - T}{TT_0}\right] \tag{14.28}$$

and

$$\tau = \tau_0 \exp\left[\frac{Q}{n_\sigma + 1}\frac{T_0 - T}{TT_0}\right], \tag{14.29}$$

where T_0 is the temperature at which the scales are δ_0 and τ_0. For $Q = 250$ kJ/mol, $n_\sigma = 3$, $\delta_0 = 31$ m, and $\tau_0 = 10$ ky, and estimating the temperature of the amphibolite facies metamorphism as $T_0 = 848$ K; the initial length and time scales increase to 780 m and 250 ky at the temperature of the brittle-ductile transition (~ 623 K). For $q_e/q_0 = \bar{q}/q_0 = 10^2$, from the initial wave speed $v_\phi/v_0 = 12.2$ (Fig. 14.8a), $V_e^{1d}/\delta_0/\phi_0 = 49$ (Fig. 14.12a) and, if $V_e^{1d}$and ϕ_0 are constant, then at the brittle-ductile transition $V_e^{1d}/\delta_1/\phi_0 = \left(V_e^{1d}/\delta_0/\phi_0\right)(\delta_0/\delta_1) = 2.0$. This value is below the minimum in $V_e^{1d}/\delta/\phi_0$, so in this case the wave would reach λ_{max} below the brittle-ductile transition, at which point it would begin to evolve toward the periodic wave solution. For the case $q_e/q_0 = \bar{q}/q_0 = 10^4$, the initial wave has $v_\phi/v_0 = 36$ and $V_e^{1d}/\delta_0/\phi_0 = 3400$, so at the brittle-ductile transition $V_e^{1d}/\delta_1/\phi_0 = 140$. From this value of $V_e^{1d}/\delta/\phi_0$ (Fig. 14.12), the quasi-steady state wave has $v_\phi/v_0 = 18$, $\lambda/\delta_1 = 7.2$, $\phi_{max}/\phi_0 = 28$, and $q_e/q_0 = 67$. As this wavelength (5,600 m) exceeds l_A it may be concluded that the flow processes would cease to be controlled by the viscous steady-state at greater depth. For this particular case, the overpressure associated with the wave (~50 MPa) near the brittle-ductile transition might be sufficient to provoke a change from viscous to plastic dilational deformation. In the absence of such a change, viscous waves are expected to die at depth, with smaller waves dying at greater depth. Death, in this context, means simply that the behavior of the system cannot be predicted in terms of the steady state. What can be predicted is that in its death throes a viscous wave will produce a sub-horizontal fluid-rich domain, with thickness comparable to l_A beneath the brittle-ductile transition.

14.5.6 Hydrofracture and Decompaction-Weakening

The viscous porosity wave mechanism requires overpressures of the same magnitude as the effective pressures that cause compaction ($\sim\lambda\Delta\rho g/2$). If these overpressures are greater than rock tensile strength, they induce plastic dilational strain by macroscopic or microscopic hydrofracturing, the latter manifestation being favored at high temperature (Hill 1950). Returning to the schematic devolatilization scenario considered in the viscous case (Fig. 14.6a), the greatest overpressures must occur at the top of the reacted horizon, thus repeated hydrofracturing will propagate porosity into the overlying rocks. Provided the hydrofracturing occurs on a length scale that is small in comparison to the viscous compaction length δ, the rate of propagation is limited by the rate at which compaction at depth supplies fluid to the hydrofracture front. Thus, in 1-d there is a steady state in which fluid driven upward through a porous domain, by viscous compaction at depth, is accommodated by hydrofracturing at overpressures that are much smaller than the effective pressures required for compaction (Fig. 14.6c). The difficulty in quantifying this steady-state is that it is dependent on details of the hydrofracture mechanism (Rozhko et al. 2007). An approximation that circumvents

this complexity is to assume that the effect of plasticity is to reduce the effective viscosity of rocks undergoing decompaction. The assumption is justified if hydrofracture and viscous dilation occur in tandem, because the effective behavior is then viscous; but characterizing this behavior by a single parameter is ad-hoc. For present purposes, the parameter chosen to characterize a relative weakening in decompaction is

$$R = \sqrt[n_\sigma+1]{A/A_\mathrm{d}}$$

where A_d is the coefficient of viscous flow during decompaction, i.e., $R < 1$. The reason for using R rather than A_d to characterize decompaction-weakening is that R is the proportionality constant that relates the length scales for decompaction and compaction, i.e., the decompaction length is $\delta_\mathrm{d} = R\delta$. If decompaction weakening maintains fluid overpressures near the tensile strength σ_y, then R is related to σ_y by

$$\sigma_\mathrm{y} = \delta_\mathrm{d}\Delta\rho g = R\delta\Delta\rho g. \tag{14.30}$$

Equation 14.30 results in a parameterization that is consistent with the expectation that overpressure is limited by the rock tensile strength, but it does not justify the formulation.

In the 1-d case, the existence of a solitary wave solution for a matrix with decompaction-weakening requires only that it is possible to connect the viscous solitary wave solution for the decompacting region, with length scale $R\delta$, with the viscous solution for the compacting region, with length scale δ. Because the relationship between wave velocity and amplitude is independent of the coefficient of viscous flow (Eq. 14.55, Appendix), this connection is possible in 1-d and identical to the viscous solitary wave solution except that the overpressured portion of the wave scales as $R\delta$ rather than δ. Compaction is the rate limiting process for the combined solution, with the result that the time scale for the steady state is unchanged from the viscous case. Moreover, for strong manifestations of plasticity, i.e., $R << 1$, the extent of the overpressured portion of the wave is insignificant, with the result that the wave solution for decompaction-weakening is well approximated by the lower half of the viscous solution. In numerical simulations, such waves appear as self-propagating fluid compartments within which fluid pressure rises along a hydrostatic gradient to pressures slightly above the lithostat (Connolly and Podladchikov 2000).

Decompaction-weakening results in a rheology in which rocks weaken in the direction of compaction-driven flow. This effect is the opposite of thermal activation in the viscous case, which leads to flattening of porosity waves (Fig. 14.11). Thus, decompaction-weakening causes waves to elongate in the direction of flow inducing channelization (Fig. 14.13). The channels are generated by tube-like porosity waves of extraordinary amplitude and speed that leave a trail of incompletely compacted porosity in their wake. These trails act as preferential pathways for subsequent fluid flow, and develop initially with spacing ~ δ and width ~ $R\delta$, a

geometry that amplifies the source fluid flux by a factor of ~ $4/R^2$. This pattern of fluid flow corresponds to that inferred in greenschist-facies rocks by Skelton et al (2000), who propose that the flow was episodic and propagated by microcracking. Similar flow patterns have also been inferred in asthenospheric systems (Jagoutz et al. 2006; Bouilhol et al. 2009; Bouilhol et al. 2011).

The tube-like waves are propagated by a region of overpressure that decompacts the matrix on the length scale "$R\delta$" (Fig. 14.13). A much larger region of underpressure of length scale δ, beneath the overpressured region, is necessary for compaction to expel fluid at the rate required to fill the porosity created by decompaction. This asymmetric pressure distribution induces unbalanced fluid circulation (Fig. 14.10b), which causes the waves to gain fluid by draining the porosity of the surrounding matrix. The gain in fluid obviates a steady state, but the speed-amplitude relation of the waves is essentially identical to the symmetric viscous case suggesting a quasi-steady state. This quasi-steady state can be explained by observing that if decompaction is much more rapid than compaction, then the decompacting region will develop with the characteristics of the upper hemisphere of the 2- or 3-d viscous solution on the length scale $R\delta$. Compaction restores the porosity generated by decompaction on the length scale δ, thus the compacting region will approximate the lower half of a prolate ellipsoid (Fig. 14.10b). The associated fluid volume is $R^2V_e^0/2$, where V_e^0 is the fluid volume of the 3-d spherical viscous solution (Eq. 14.27), which is approximated by applying spherical symmetry to the porosity distribution of the 1-d viscous solution. For R in the range $10^{1/2}$– 10^3 this model has been verified by comparison with numerical simulations for linear viscous rheology ($n_\sigma = 1$, Connolly and Podladchikov 2007). These simulations also show that, in the absence of thermal effects, wave amplitude grows as

$$\partial\phi_{\max}/\partial t \approx \phi_0 \Big/ \left(\tau R^{3/4}\right). \tag{14.31}$$

and that the speed-amplitude relation of waves is essentially identical to the steady solitary wave solution in a viscous matrix without decompaction-weakening if the simple viscous matrix is characterized by the $AR^{n_\sigma+1}$. This latter result implies that the effective time-scale for compaction-driven fluid flow in a decompaction-weakening matrix is dictated by the viscous response of the weak, overpressured, rocks, i.e., the effective time-scale is

$$\tau_d \approx \tau R. \tag{14.32}$$

Given the ad-hoc nature of the parameterization further quantification is unwarranted, but the role of plastic yielding should increase with falling temperature because δ is strongly dependent on temperature, but yield strength is weakly temperature dependent. Thus, a decompaction-weakening rheology causes compaction-driven fluid flow to become increasingly focused towards the surface, the antithesis of the behavior of the symmetric viscous case.

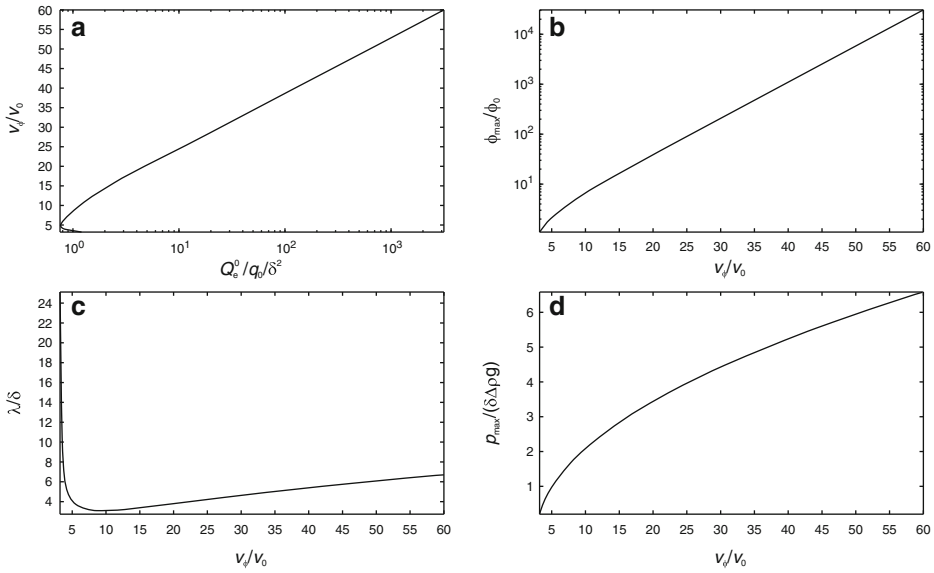

Fig. 14.14 Quasi-steady state solitary wave properties (for $n_\sigma = n_\phi = 3$) for a decompaction-weakening viscous rheology as a function of Q_e^0. For $R << 1$, the volumetric rate of fluid transport by a wave is $Q_e \approx Q_e^0 R^2$. Equating this rate to the source flux that is focused into the wave, $Q_s \approx 4\bar{q}\delta^2$, yields the value of $Q_e^0/\delta^2 q_0$(i.e., $4\bar{q}/R^2 q_0$). This value is appropriate to predict the properties of the 3-d tube-like waves that would nucleate from a dehydrating horizon

Decompaction weakening causes fluid flow within a horizontal source region to be focused into tube-like channels of width $R\delta$ with a characteristic spacing δ. The properties of the waves responsible for channel formation can be predicted as a function of R and fluid production within the source region if, as before, a balance between fluid transport and production is assumed. The symmetry of the quasi-steady state is such that for $R << 1$ the rate of fluid transport, by a wave, is $Q_e \approx Q_e^0 R^2$, where $Q_e^0 = V_e^0 v_\phi/\lambda/2$ is half the rate for the viscous rheology ($R = 1$). Approximating the area drained by a channel as a square of area $4\delta^2$, the vertically-integrated fluid production rate within the source region is $Q_s \approx 4\bar{q}\delta^2$. Equating Q_e and Q_s, rearranging the result, and dividing through by q_0 to make the result non-dimensional, yields

$$\frac{Q_e^0}{\delta^2 q_0} \approx \frac{4\bar{q}}{R^2 q_0}. \tag{14.33}$$

Given Q_e^0 from Eq. 14.33, wave speed, amplitude, and wavelength, which are independent of R, are recovered from the properties of the steady-state (Fig. 14.14). In the absence of experimental or theoretical constraints, field evidence of channelized fluid flow can be used to infer the R values necessary to explain

channelization by decompaction weakening. Channelization patterns are difficult to discern at low metamorphic grades, but at higher temperatures patterns associated incipient charnockitization (Stahle et al. 1987) and pervasive melt migration (Jagoutz et al. 2006; Bouilhol et al. 2009; Bouilhol et al. 2011) are broadly consistent with $R \sim O(10^{-1})$. Adopting this value for the scales of the amphibolite facies example considered previously ($\delta = 31$ m and $\tau = 10$ ky), a miniscule flux perturbation of $\bar{q}/q_0 = 2$ ($Q_e^0/\delta^2/q_0 = 800$) is adequate to generate a wave that travels with speed $v_\phi = 51\ \delta/\tau = 160$ m/ky, vertical dimension $\lambda = 6\delta = 190$ m, horizontal dimension $R\lambda = 19$ m, $\phi_{max} = 0.7$, $p_{max} = 4$ MPa ($\sim\lambda\Delta\rho g$), and $p_{min} = -0.4$ MPa ($\sim R\lambda\Delta\rho g$). Although the amplitude of this wave violates the small-porosity approximation used to derive the steady-state properties, it demonstrates the extraordinary efficacy of 3-d focusing. In nature, such instabilities would be likely to provoke an alternative transport mechanism such as fracture-controlled flow.

14.6 Adding Details

The suggestion that lower crustal fluid flow is accomplished by the propagation of fluid-rich domains that correspond to some esoteric solution of the compaction equations cries for evidence and provokes the suspicion in the minds of field-based geologists that they are being sold a geological analog to the proverbial spherical cow of theoretical physics. The model is the mathematical consequence of a set of essential assumptions that are, at least individually, accepted in geoscience; the purpose of this Chapter is to draw attention to this consequence rather than to prove that it corresponds to reality. If there is a spherical cow to be found, then it must be lurking among these assumptions. The assumptions are: (1) that when a fluid is present its pressure is near lithostatic; (2) that flow is governed by Darcy's law; (3) that permeability is continuous and a strong function of connected porosity; and (4) that compaction occurs by a viscous mechanism (e.g., dislocation or pressure-solution creep) in response to effective pressure. In rejecting the model, it behooves the skeptic to decide which of these assumptions is false. The fourth assumption is treacherous at small porosities because omnipresent elastic mechanisms may limit viscous response (Connolly and Podladchikov 1998; Bercovici et al. 2001). However, if these assumptions are accepted, the consequence is that fluid flow must be episodic and accompanied by oscillations in fluid pressure, even in an idealized homogeneous crust perturbed by an idealized devolatilization reaction. As a prediction, this result is mundane because there is no geologic evidence to the contrary; its value is only that it offers a consistent explanation for such phenomena that, in principle, can be tested against observation. The purpose of modeling is not to emulate the complexity of nature, rather to explain it. For this reason, the models presented here sacrifice detail, but it is undeniable that the details of natural systems will influence fluid flow. A comprehensive discussion of this influence is

impractical; however, it is appropriate to consider some circumstances when the effect of such details can be neglected or anticipated.

14.6.1 Large-Scale Lateral Fluid Flow

Metamorphic devolatilization reactions have the capacity to produce high porosity layers, within which the compaction length, δ_1, may be orders of magnitude greater than it is in the surrounding rocks. In principle such a layer has the capacity to conduct lateral fluxes on the length scale δ_1; however, in the absence of external forcing, the pressure gradients responsible for lateral fluxes are limited by the spacing of the porosity waves that effect drainage through the low porosity surroundings. This spacing is dictated by the compaction length in the unperturbed matrix, which therefore determines the length scale for lateral fluid flow (Figs. 14.9 and 14.13). It seems probable that large-scale lateral fluid flow inferred from metamorphic field studies (e.g., Ferry and Gerdes 1998; Skelton 1996; Wing and Ferry 2007) is induced by external perturbations, such as drainage caused by tectonically-induced dilatant shear zones (Sibson 1992) or mean stress variations caused by folding (Schmalholz and Podladchikov 1999; Mancktelow 2008). The strength of these perturbations increases rock strength, thus they are likely to become important under the same conditions that embrittlement may cause a decompaction-weakening rheology (Sect. 14.5.6). Because decompaction weakening reduces the time-scale for dynamic drainage by porosity waves through the unperturbed matrix, the influence of an externally imposed drain will be dependent on the relative magnitudes of the time scale for within-layer flow

$$\tau_1 = \tau_0 \left(\frac{\phi_0}{\phi_1} \right) \phi_0^{\frac{n_\sigma \left(n_\phi - 1 \right)}{n_\sigma + 1}} \tag{14.34}$$

and the effective time scale τ_d (Eq. 14.32) for dynamic drainage by decompaction weakening, such that the process that operates on the shorter time-scale will dominate (Fig. 14.15). For the case $\tau_1 = \tau_d$, numerical simulation of fluid flow caused by the intersection of a permeable fracture zone with a metamorphic reaction front (Fig. 5 of Connolly 2010) shows that lateral flow occurs toward the fracture zone on the length scale δ_1 for $t < \tau_d$, but occurs only on the shorter length scale δ_0, and is independent of the fracture zone, at $t > \tau_d$. It is of course possible that a reaction generates a highly permeable layer that is sealed from above by a different, impermeable, lithology. In this case, the lateral flow can occur on the length scale δ_1. As evidence for large-scale lateral flow appears to come primarily from low and moderate grade metamorphic rocks, a more probable explanation for the phenomenon is that the flow occurs at conditions such that $\delta < l_A$. Under such conditions (Fig. 14.11), the vertical scale for compaction driven flow is l_A, but the horizontal length scale is the local value of δ, which increases exponentially with falling temperature.

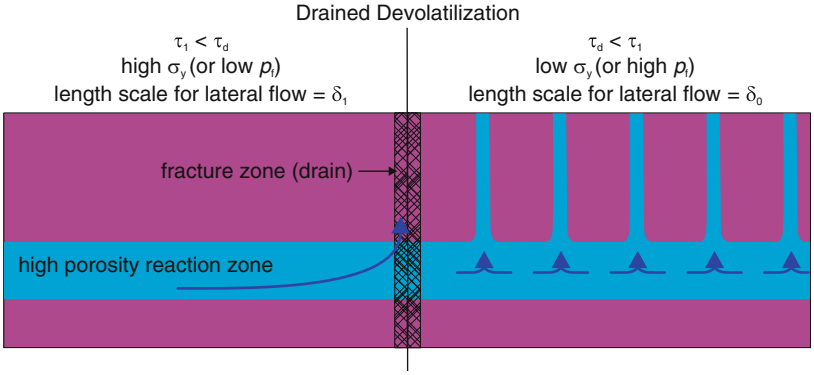

Fig. 14.15 Schematic of the influence of a drain (e.g., a permeable fracture zone) on fluid flow within a high porosity horizon generated by a devolatilization reaction. If the compaction time and length scales in the unperturbed matrix are τ_0 and δ_0, and the porosity in the horizon is ϕ_1, then the corresponding scales within the horizon are, for $n_\sigma = n_\phi = 3$, $\delta_1 = (\phi_1/\phi_0)^{1/2}\delta_0 > \delta_0$ and $\tau_1 = (\phi_0/\phi_1)^{3/2}\tau_0 < \tau_0$. Thus, in the absence of decompaction weakening, the drain will draw fluid from the layer on the length scale δ_1 (as depicted to the left of the drain) because the time scale (τ_1) for within layer flow is shorter than the time scale (τ_0) for the development of dynamic drainage within the unreacted matrix in response to high fluid pressure. If tensile yield strength is $< \delta_0\Delta\rho g$, then decompaction weakening reduces the time scale for the development of dynamic drainage to $\tau_d = \sigma_y/(\delta_0\Delta\rho g)\tau_0$. Thus, decompaction weakening may lead to circumstances (i.e., $\tau_d < \tau_1$) in which dynamic drainage dominates and the length scale for lateral fluid within the layer is limited by the compaction length (δ_0) in the unreacted rocks

14.6.2 Lithological Heterogeneity

There are two limiting cases for lithological heterogeneity. The trivial case is that the heterogeneity occurs on length scales that are $>> \delta$. In this case (Fig. 14.16a), the time and length scales relevant for each lithology individually dictate compaction phenomena. The alternative is that the heterogeneities are small, relative to the compaction length, in any of the individual lithologies. To illustrate this case (Fig. 14.16b), suppose a vertical sequence of two alternating lithologies in which the layering is thin compared to the compaction length in either layer and that the compaction length in one layer is so much larger than in the other layer that is effectively infinite (i.e., the lithology is rigid). If a porosity wave impinges on such a sequence, the fluid pressure gradient within the rigid layer must rise to supra-lithostatic values to conduct the excess flux carried by the wave, but within the soft layers dilation will cause the fluid pressure gradient to relax to near hydrostatic values in regions of elevated porosity. The result is to create a stepped fluid pressure profile that maintains a balance between compaction and dilation on the compaction time and length scales of the soft lithology. An implication of this behavior is that the effective rheology for compaction processes in the lower crust is dictated by the rheology of the weakest lithology. In contrast, crustal strength in response to tectonically imposed deformation may be controlled by the strongest lithology, i.e., in the case of homogeneous thickening or thinning.

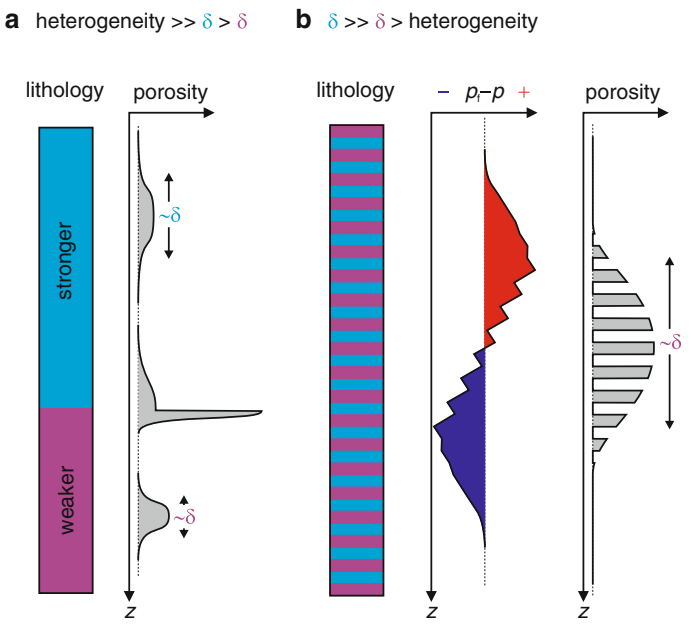

Fig. 14.16 Schematic of the influence of lithological layering on the propogation of a solitary porosity wave through a viscous matrix. If the layers are thick, compared to the compaction length, within each layer (**a**), the wave adopts its shape and speed according to the local compaction time and length scales. If the layers are thin compared to the compaction length in either lithology, but the compaction length is much greater in one lithology than it is in the other (**b**), then the properties of the wave are limited by the compaction scales in the weaker lithology. The effective pressure profile is drawn so that the fluid pressure gradient in the large porosity weak layers is near hydrostatic, and that fluid pressure gradient necessary to conduct the excess flux within the intervening rigid layers is supralithostatic and constant. In reality, because the excess flux varies locally within a solitary wave, the supralithostatic gradients in the rigid layer would decrease toward the tails of the wave

14.6.3 Non-Lithostatic Stress

Compaction-driven flow responds to tectonic stress through its dependence on the mean stress gradient (Eq. 14.5), but local deformation and/or lithological heterogeneity may give rise to strong variations in the far-field stress (Schmalholz and Podladchikov 1999; Mancktelow 2008). As in the case of lithological heterogeneity in a lithostatic crust, the influence of these variations depends upon whether they occur on a spatial scale that is large or small compared to the compaction length scale. Small scale variations will affect local flow patterns, but will not influence the overall tendency of compaction to drive fluid toward low mean stress (strictly in the direction of $\rho_f \mathbf{g}\mathbf{u}_z - \nabla\bar{\sigma}$, which is vertical in the lithostatic limit). These variations may distort the geometry of the porosity waves that develop in the non-lithostatic case. But because the effective pressure necessary for compaction can only be

achieved by having hydraulic connectivity on the compaction length scale, the distortions are likely to be primarily kinematic.

Large scale tectonic perturbations to the lithostatic mean stress gradient can, in general, be expected to have relatively minor influence on the rate and direction of compaction-driven fluid flow. The greatest influence on rate is realized during extension. In such a setting, the relaxation of differential stress in the brittle crust, which may be comparable to half the vertical load (Ranalli 1995), will relax over an $O(l_A)$ vertical interval (Connolly and Podladchikov 2004), potentially increasing the mean stress gradient responsible for, and accelerating, compaction-driven fluid flow. Perhaps more importantly, this effect will be amplified within, and favor the formation of, vertically elongated hydraulic domains such as the porosity waves predicted for the decompaction-weakening rheology (Sect. 14.5.6). The greatest influence on direction is realized in compression. During tectonic compression, the brittle crust supports differential stresses that are approximately twice the lithostatic load (Petrini and Podladchikov 2000; Mancktelow 2008). The relaxation of this stress gives rise to a negative mean stress gradient that may cause downward directed compaction-driven fluid flow on an $O(l_A)$ scale (Connolly and Podladchikov 2004). The inversion also creates a barrier to upward directed compaction driven flow. This barrier is most effective within vertically elongated hydraulic domains; thus, in contrast to the extensional case, compression may favor the formation of slow moving, horizontal, hydraulic domains such as the porosity waves predicted for compaction-driven flow in upward strengthening viscous rocks (Sect. 14.5.5).

In the lithostatic limit, rocks can sustain fluid overpressures comparable to their tensile strength. Thus, decompaction can occur by viscous mechanisms as assumed in the porosity wave models presented here. However, in the presence of large differential stresses, rocks will fail by plastic mechanisms before the fluid overpressure necessary for viscous dilational mechanisms can develop (Sibson 2000; Rozhko et al. 2007). As differential stresses are expected to grow towards the brittle-ductile transition, plastic failure will limit the viscous porosity wave mechanism to greater depths in non-lithostatic settings. Whether truly brittle deformation can be propagated upward by viscous compaction at depth, as implied by the viscous decompaction-weakening model advocated here, remains to be demonstrated.

14.7 Concluding Remarks

At near surface conditions, tectonic deformation maintains permeable fracture systems that, under most circumstances, permit drainage of crustal fluids with negligible fluid overpressure (e.g., Zoback and Townend 2001). In this regime, fluid flow is largely independent of the stress state of the rock matrix and weak perturbations induced by topography or fluid density variations may give rise to complex flow patterns (e.g., Ingebritsen et al. 2006). The base of the seismogenic

zone, at temperatures of ~ 623 K, defines the brittle-ductile transition (Sibson 1986; Scholz 1988), but evidence for the involvement of high pressure fluids in faulting (e.g., Sibson 2009; Cox and Ruming 2004; Miller et al. 2004) indicates that fluid overpressures develop above the brittle-ductile transition on the inter-seismic time scale. This short-term cyclicity reflects the role of localized compaction in sealing faults and fractures (Gratier et al. 2003; Tenthorey and Cox 2006). But at the brittle-ductile transition the time scale for fluid expulsion ($> 2.3\ c_\sigma/\dot{\varepsilon}_{\text{tectonic}} \sim O(10^8)$ y) is slow with respect to metamorphic fluid production. Thus, the brittle-ductile transition lies within a transitional hydrological regime in which compaction-driven fluid flow is gradually superimposed on the upper crustal regime. Within this transitional regime, the efficiency of compaction increases exponentially with depth on the $O(1)$ km scale of the viscous e-fold length (Fig. 14.1). Because the efficiency of compaction must be measured relative to rates of fluid production or drainage, it is not possible to make a general statement about the depth or temperature at which metamorphic fluid flow will become dominated by compaction.

Even if recent challenges (e.g., Oliver et al. 2000; Dewey 2005; Ague and Baxter 2007) to the paradigm of heat-conduction limited metamorphism (England and Thompson 1984) are acknowledged, the development of high fluid pressures indicates that metamorphic environments must be characterized by extraordinarily low permeability. Metamorphic fluid expulsion is not necessarily efficient (Warren et al. 2011), but efficient fluid expulsion from poorly drained rocks requires a dynamic mechanism in which the dilational deformation responsible for increasing permeability is balanced by a compaction mechanism at depth responsible for maintaining high fluid pressure. An essential feature of such a mechanism is that, irrespective of the mean-stress gradient, hydraulic connectivity must be maintained over a vertical interval that is large enough to generate the effective pressures necessary to drive the deformation. Both self-propagating domains of fluid-filled fractures (Gold and Soter 1985) and individual hydrofractures (Rubin 1995; Nakashima 1995; Okamoto and Tsuchiya 2009) have been proposed as the mechanism for such flow. These models suppose that the fractures are closed at depth, i.e., compacted, by the elastic response of the matrix. As a consequence, the fractures propagate at high speeds, $O(1)$ m/s, and have km-scale vertical dimensions. The porosity wave mechanism, reviewed here, may also be manifest as interconnected fractures, provided the individual fractures are small in comparison to the viscous compaction length, but differs from elastic fracture models in that compaction is viscous. A satisfying feature of the viscous mechanism is that it can operate on the grain-scale, thereby explaining the pervasive compaction evident in metamorphic rocks. If viewed as competing mechanisms, the mechanism that requires the smallest vertical extent necessary to accommodate fluid production will dominate. The albeit highly uncertain $O(100)$ m estimate for the viscous compaction length, obtained here for amphibolite-facies conditions, indicates that porosity waves can meet this criterion for dominance.

The relatively minor role of compaction in many near surface environments makes large scale hydrological modeling of the upper crust possible (e.g., Ingebritsen et al. 2006). Possible in this context means that a stable initial condition can be

envisioned in which fluid and rock coexist. In contrast, the lower crust is an environment in which fluids are mechanically and, potentially, thermodynamically unstable (Connolly and Thompson 1989). Thus there is no time-invariant initial condition from which it is possible to assess the impact of the metamorphic process, which is itself the most likely source of lower crustal fluids. The assertion that the lower crust has an intrinsic background permeability towards which transient permeability decays is logically specious, because it is based on time-averaged metamorphic fluxes. However, permeabilities inferred from time-averaged fluid fluxes do provide an upper limit on the background permeability that characterizes the local environment of a metamorphic process in time and space (Ingebritsen and Manning 2010). The time and length scales for viscous compaction have been formulated to emphasize this limitation by separating material properties of the solid and fluid, from two transient properties of the initial state, namely porosity and the hypothetical background flux necessary to maintain lithostatic fluid pressure. If the time-averaged flux is used in place of the background flux, then the result provides only upper and lower limits on the compaction length and time scales. Consequently, forward models are unlikely to reveal the scales of fluid flow in lower crustal systems, but observations of natural patterns may ultimately provide a useful parameterization of these scales. These scales are fundamental limits for flow phenomena that are independent of stress state within the solid matrix. Thus, the scales are constrained by the duration and extent of lateral (e.g., Ferry and Gerdes 1998; Wing and Ferry 2007; Staude et al. 2009) or downward (e.g., Austrheim 1987; McCaig et al. 1990; Wickham et al. 1993; Upton et al. 1995; Cartwright and Buick 1999; Read and Cartwright 2000; Gleeson et al. 2000; Yardley et al. 2000; Munz et al. 2002; Gleeson et al. 2003) fluid flow.

The role of compaction in metamorphic fluid flow is extraordinarily uncertain, but ignoring this uncertainty in models of metamorphic fluid flow does not make the models any more certain. Compaction is a good news, bad news story. The bad news is that the details of lower crustal flow may be influenced by unknowable details. The good news is that compaction driven fluid flow has a tendency to self-organize. Self-organization eliminates the dependence on details that are present on spatial or temporal scales that are smaller than the compaction length and time scales. Porosity waves are the mechanism for this self-organization, through which dilational deformation is localized in either time and/or space to create pathways for fluid expulsion. Although, this dilational deformation may be manifest as plastic failure, its rate is limited by the compaction process necessary to maintain elevated fluid pressures. At metamorphic conditions, the compaction process is unequivocally viscous. The porosity waves that form in a matrix that compacts by viscous mechanisms are generally solitary waves that, once formed, are independent of their source. This chapter has outlined a simple method of predicting the geometry, size, and speed of such waves under the assumption that fluid drainage keeps pace with fluid production. If this assumption were true throughout the metamorphic column then the time-averaged permeability would be identical to that obtained by assuming uniform fluid flow. In fact, the assumption is demonstrably untrue on a crustal scale for the viscous case, because the waves slow towards the brittle-ductile transition,

an effect that leads to fluid accumulation. Of course, the activation of other drainage mechanisms may maintain the assumed steady state, but the inconsistency serves to demonstrate that characterizing a dynamic system by a time-averaged dependent property, such as permeability, has no predictive value.

In the viscous limit, the models summarized here predict that lower crustal porosity waves will create fluid-rich horizons, with thickness comparable to l_A, beneath the brittle-ductile transition (Sect. 14.5.5). Geophysical evidence for such horizons is common (Suetnova et al. 1994; Hammer and Clowes 1996; Ozel et al. 1999; Liotta and Ranalli 1999; Makovsky and Klemperer 1999; Vanyan and Gliko 1999; Stern et al. 2001; Jiracek et al. 2007). Coupled with external forcing, the horizons may function as conduits for the large-scale lateral fluid flow responsible for some types of hydrothermal mineralization and as reservoirs for fluid-driven seismicity (e.g., Cox 2005). Paradoxically, although these horizons reflect upward strengthening of the ductile crust with respect to dilational processes, they may reduce the shear strength of the crust precisely at depths where the crust is presumed to be strong. Fluid flow within this interval of the crust is likely to be further complicated by the influence of tectonic stress developed in the brittle crust (Sect. 14.6.3). To make matters still worse, elastic compaction mechanisms become competitive at this depth (e.g., Fig. 14.15 of Connolly and Podladchikov 1998). Elastic compaction rheology also has wave solutions that form in response to high fluid pressures (Rice 1992), but unlike viscous waves, elastic waves cannot detach from their source and propagate as transient shocks accompanied by fluid pressure surges. Thus, the stagnation of mid-crustal viscous porosity waves may be accompanied by high velocity, low amplitude surges of fluid into the upper crust (Connolly and Podladchikov 1998). This type of flow pattern is consistent with the timing of aftershocks during crustal faulting (Miller et al. 2004). Because elastic waves can propagate through a matrix with no prior hydraulic connectivity, elastic compaction may also be an important mechanism at the onset of metamorphism. Viscoelastic porosity wave solutions exist in the zero-porosity limit (Connolly and Podladchikov 1998), but their relevance to metamorphic fluid expulsion has yet to be explored.

Porosity waves are a mechanism capable of bridging the extremes between pervasive and fully segregated fluid flow. The metasomatic effect of fluid infiltration is maximized between these extremes when the flow is strongly focused into channels, but not fully segregated. A decompaction-weakening matrix rheology, in which the matrix yields more readily under negative effective pressure than it does under positive pressures, can explain channeling (Sect. 14.5.6). The origin of this rheology is attributed to the asymmetric role of cohesion during dilation (Connolly and Podladchikov 2007). The expression of plastic yielding is temperature-dependent, tending toward the ductile and brittle limits at, respectively, high and low temperatures (Hill 1950). Thus at high temperatures decompaction-weakening is capable of inducing channelized fluid flow in completely ductile rocks (Bouilhol et al. 2011). Reactive transport instability (Daines and Kohlstedt 1994; Aharonov et al. 1997) and shear-enhanced segregation (Holtzman and Kohlstedt 2007) are alternative mechanisms for inducing channelization in ductile rocks. In nature any

mechanism of channelization may be associated with metasomatism, but the reactive transport instability is implicitly metasomatic. A limitation to the reactive transport instability is that the net solubility of the matrix in the fluid must increase in the direction of fluid flow. The key distinction between the flow patterns generated by decompaction-weakening and other focusing mechanisms, is that in the case of decompaction-weakening fluid is circulated into and out of the matrix, whereas reactive transport and shear-enhanced segregation are associated with unidirectional flow. When considered in tandem, mechanical and reactive transport instabilities are mutually reinforcing (Spiegelman et al. 2001; Liang et al. 2010).

Acknowledgements This paper was improved by outstanding, although not necessarily laudatory, reviews by Stephen F. Cox, Yves Gueguen, Peter O. Koons and Peter I. Nabelek. I am grateful to Dan Harlov and Hakon Austrheim for their extraordinary patience and judicious editing. The work presented here was supported by Swiss National Science Foundation grant 200021_130411.

Appendix: Steady-State Porosity Waves in a Viscous Matrix

This appendix presents a steady-state wave solution for flow of an incompressible fluid through a viscous matrix composed of incompressible solid grains. Geological compaction literature invariably assumes Newtonian behavior for the viscous mechanism; however, lower crustal environments may well be characterized by power-law viscous rheology (e.g., Kohlstedt et al. 1995). Accordingly, the solution derived here is general with respect to the dependence of the viscous rheology on effective pressure. Aside from this modification, the mathematical formulation of the governing compaction equations is identical to that of Connolly and Podladchikov (2000, 2007).

Conservation of solid and fluid mass requires

$$\frac{\partial(1-\phi)}{\partial t} + \nabla \cdot ((1-\phi)\mathbf{v}_\mathrm{s}) = 0 \tag{14.35}$$

and

$$\frac{\partial \phi}{\partial t} + \nabla \cdot (\phi \mathbf{v}_\mathrm{f}) = 0, \tag{14.36}$$

where subscripts f and s distinguish the velocities, $\mathbf{v}$, of the fluid and matrix. From Darcy's law, force balance between the matrix and fluid requires

$$\mathbf{q} = \phi(\mathbf{v}_\mathrm{f} - \mathbf{v}_\mathrm{s}) = -\frac{k}{\mu}(\nabla p_\mathrm{f} - \rho_\mathrm{f} g \mathbf{u}_z). \tag{14.37}$$

In one-dimensional compaction of a vertical column, mean stress is identical to the load

$$\bar{\sigma} = \int_0^z ((1-\phi)\rho_s + \phi\rho_f) g \mathbf{u}_z dz. \tag{14.38}$$

Thus, in terms of effective pressure, $p_e = \bar{\sigma} - p_f$, Eq. 14.37 is

$$\phi(\mathbf{v}_f - \mathbf{v}_s) = \frac{k}{\mu}(\nabla p_e - (1-\phi)\Delta\rho g \mathbf{u}_z). \tag{14.39}$$

The divergence of the total volumetric flux of matter is the sum of Eqs. 14.35 and 14.36

$$\nabla \cdot (\mathbf{v}_s + \phi(\mathbf{v}_f - \mathbf{v}_s)) = 0, \tag{14.40}$$

and substituting Eq. 14.39 into Eq. 14.40

$$\nabla \cdot \left(\mathbf{v}_s + \frac{k}{\mu}(\nabla p_e - (1-\phi)\Delta\rho g \mathbf{u}_z) \right) = 0. \tag{14.41}$$

Matrix rheology is introduced with Eq. 14.16 by observing that the divergence of the solid velocity is the dilational strain rate of the matrix

$$\nabla \cdot \mathbf{v}_s = \frac{\phi}{1-\phi}\dot{\varepsilon}_\phi = -c_\alpha f_\phi A |p_e|^{n_\sigma - 1} p_e \tag{14.42}$$

where $f_\phi = \phi(1-\phi)/\left(1-\phi^{1/n_\sigma}\right)^{n_\sigma}$ (Wilkinson and Ashby 1975). As the functional form of Eq. 14.42 may vary depending on the magnitude of the porosity and the viscous mechanism (Ashby 1988), the subsequent analysis assumes f_ϕ is an unspecified function of porosity.

To avoid the unnecessary complication associated with the use of vector notation for a one-dimensional problem, in the remainder of this analysis vector quantities are represented by signed scalars and the gradient and divergence operators are replaced by $\partial/\partial z$. Supposing the existence of a steady state solution in which fluid explusion is accomplished by waves that propagate with unchanging form through a matrix with background porosity ϕ_0 filled by fluid at zero effective pressure, then, in a reference frame that travels with the wave, integration of Eq. 14.35 gives the matrix velocity as

$$v_s = v_\infty \frac{1-\phi_0}{1-\phi} \tag{14.43}$$

where v_∞ is the solid velocity in the limits $\phi \to \phi_0$ and $p_e \to 0$, i.e., at infinite distance from the wave. After substitution of Eq. 14.43, the integrated form of Eq. 14.41 can be rearranged to

$$\frac{\partial p_e}{\partial z} = \left(q_t - v_\infty \frac{1-\phi_0}{1-\phi} \right) \frac{\mu}{k} + (1-\phi)\Delta\rho g \tag{14.44}$$

where $q_t = \phi v_f + (1-\phi)v_s$ is the constant, total, volumetric flux of matter through the column, which evaluates in the limit $\phi \to \phi_0$ and $p_e \to 0$ as

$$q_t = v_\infty - (1-\phi_0)\frac{k_0}{\mu}\Delta\rho g \tag{14.45}$$

where k_0 is the permeability at ϕ_0. Thus, Eq. 14.44 can be rewritten

$$\frac{\partial p_e}{\partial z} = \Delta\rho g \left(1 - \phi - (1-\phi_0)\frac{k_0}{k} \right) - v_\infty \frac{\mu}{k} \frac{\phi - \phi_0}{1-\phi}. \tag{14.46}$$

Likewise, substitution of Eq. 14.43 into Eq. 14.42 yields

$$\frac{\partial \phi}{\partial z} = -\frac{(1-\phi)^2}{1-\phi_0} f_\phi \frac{c_\sigma A |p_e|^{n_\sigma - 1} p_e}{v_\infty} \tag{14.47}$$

If permeability is an, as yet unspecified, function of porosity, then Eqs. 14.46 and 14.47 form a closed system of two ordinary differential equations in two unknown functions, ϕ and p_e. As v_∞ is the solid velocity at infinite distance from a steady-state wave, if the reference frame is changed to that of the unperturbed matrix, the phase velocity of the wave is $v_\phi = -v_\infty$.

For notational simplicity Eqs. 14.46 and 14.47 are now rewritten as

$$\frac{\partial p_e}{\partial z} = f_1 \tag{14.48}$$

$$\frac{\partial \phi}{\partial z} = f_2 \frac{c_\sigma A}{v_\phi} |p_e|^{n_\sigma - 1} p_e \tag{14.49}$$

where f_1 is the dependence of Eq. 14.46 on ϕ and v_ϕ, and f_2 isolates the dependence of Eq. 14.47 on ϕ. Combining Eqs. 14.48 and 14.49 to eliminate z, and rearranging, yields

$$0 = \frac{c_\sigma A}{v_\phi} |p_e|^{n_\sigma - 1} p_e \mathrm{d}p_e - \frac{f_1}{f_2} \mathrm{d}\phi, \tag{14.50}$$

which must be satisfied by the ϕ-p_e trajectory of any steady-state solution. Defining a function H such that

$$H \equiv -\int \frac{f_1}{f_2} \mathrm{d}\phi, \tag{14.51}$$

the integral of Eq. 14.50 yields a function

$$U \equiv \frac{c_\sigma A}{v_\phi} \frac{|p_e|^{n_\sigma - 1} p_e^2}{n_\sigma + 1} + H \tag{14.52}$$

whose ϕ-p_e contours explicitly define the ϕ-p_e trajectory for all steady-state solutions as a function v_ϕ. Because U increases monotonically, and symmetrically, with positive or negative p_e at constant ϕ, and H is independent of p_e, the stationary points of U must occur at $p_e = 0$ and correspond to extrema in H, i.e., the real roots of $\partial H/\partial\phi = -f_1/f_2 = 0$. Moreover, as f_2 must be finite if the matrix is coherent, the roots of $\partial H/\partial\phi = 0$ are identical to the roots of $f_1 = 0$. Therefore ϕ_0 is always a stationary point, with the character of a focal point if $\partial f_1/\partial\phi < 0$ and that of a saddle point if $\partial f_1/\partial\phi > 0$. When ϕ_0 is a focal point, the steady-state wave solutions correspond to periodic waves that oscillate between two values of porosity on either side of ϕ_0, characterized by equal H, at which p_e vanishes (Fig. 14.6b). The case of greater interest is a solitary wave (Fig. 14.6a), in which the porosity rises from ϕ_0 to a maximum, at which $H(\phi_{max}) = H(\phi_0)$, and then returns to ϕ_0. This solution requires both the existence of a focal point at $\phi > \phi_0$ and that ϕ_0 is a saddle point. For the rheological constitutive relation employed here (Eq. 14.42), the first condition is always met when ϕ_0 is a saddle point. Thus, the critical velocity for the existence of the solitary wave solution, i.e., the bifurcation at which ϕ_0 switches from focal to saddle point, is

$$v_\phi^{crit} = -\frac{k_0}{\mu}(1-\phi_0)\Delta\rho g\left(\frac{(1-\phi_0)}{k_0}\left.\frac{\partial k}{\partial\phi}\right|_{\phi=\phi_0} - 1\right), \tag{14.53}$$

which is obtained by solving $\partial f_1/\partial\phi = 0$ for v_ϕ. Substituting the explicit function for permeability given by Eq. 14.17 into Eq. 14.53 yields

$$v_\phi^{crit} = -\frac{k_0}{\phi_0\mu}(1-\phi_0)\Delta\rho g\big((1-\phi_0)n_\phi - \phi_0\big) = v_0\big((1-\phi_0)n_\phi - \phi_0\big). \tag{14.54}$$

Equation 14.54 implies that, in the small-porosity limit, the minimum speed at which steady solitary waves exist is n_ϕ times the speed of the fluid through the unperturbed matrix.

The relation between solitary wave amplitude (maximum porosity) and v_ϕ is obtained by solving

$$H(\phi_{\max}) - H(\phi_0) = -\int_{\phi_0}^{\phi_{\max}} \frac{f_1}{f_2} \mathrm{d}\phi = 0. \tag{14.55}$$

The resulting expressions are cumbersome, but, in the small-porosity limit of Eqs. 14.17 and 14.42, the solution of Eq. 14.55 is

$$v_\phi = -\frac{c_\phi \phi_0^{n_\phi - 1} \Delta\rho g}{\mu} (n_\phi - 1) \frac{\phi_0^{n_\phi} + \phi_{\max}^{n_\phi} \left[n_\phi \ln\left(\frac{\phi_{\max}}{\phi_0}\right) - 1 \right]}{\phi_0^{n_\phi - 1} \left[n_\phi \phi_{\max} - \phi_0 (n_\phi - 1) \right] - \phi_{\max}^{n_\phi}}. \tag{14.56}$$

From Eq. 14.56 it follows that $n_\phi > 1$ is a necessary condition for the existence of solitary waves. Equation 14.56 also has the surprising implication that amplitude is not a function of n_σ, for large porosity the function f_ϕ, in the exact form of Eq. 14.42, gives rise to a weak dependence of amplitude on n_σ. For a solitary wave with specified phase velocity, the effective pressure is obtained as an explicit function of ϕ from the definite integral of Eq. 14.50, which can be rearranged to

$$p_e = \pm \sqrt[n_\sigma + 1]{(n_\sigma + 1) \frac{v_\phi}{c_\sigma A} \int_{\phi_0}^{\phi} \frac{f_1}{f_2} \mathrm{d}\phi}, \tag{14.57}$$

where the signs have been dropped in view of the symmetry of the solution. And finally, substituting Eq. 14.57 into Eq. 14.47, inverting the result, and integrating yields the depth coordinate relative to the center of a wave as a function of ϕ

$$z = \pm \sqrt[n_\sigma + 1]{\frac{v_\phi}{c_\sigma A (n_\sigma + 1)^{n_\sigma}}} \int_{\phi_{\max}}^{\phi} \frac{1}{f_2} \left(\int_{\phi_0}^{\phi} \frac{f_1}{f_2} \mathrm{d}\phi \right)^{-\frac{n_\sigma}{n_\sigma + 1}} \mathrm{d}\phi. \tag{14.58}$$

To demonstrate that $z \to \pm\infty$ as $\phi \to \phi_0$, the inner integral and its factor in Eq. 14.58 are approximated by the first non-zero terms of Taylor series expansions about $\phi = \phi_0$ to obtain

$$z \approx \pm \left(\frac{v_\phi}{c_\sigma A f_2|_{\phi=\phi_0}} \left(\frac{n_\sigma + 1}{2} \frac{\partial f_1}{\partial \phi}\bigg|_{\phi=\phi_0} \right)^{-n_\sigma} \right)^{\frac{1}{n_\sigma + 1}} \int_{\Phi}^{0} \Phi^{-\frac{2n_\sigma}{n_\sigma + 1}} \mathrm{d}\Phi \tag{14.59}$$

where $\Phi = \phi - \phi_0$. In the limit $\Phi \to 0$, the integral in Eq. 14.59 is finite only if $n_\sigma < 1$, from which it is concluded that solitary waves have infinite wavelength in a linear or shear thinning viscous matrix, but may have finite wavelength in the peculiar case of a shear thickening viscous matrix. Rewriting the integral in Eq. 14.59 in terms of $\mathrm{d}\ln\phi$, and differentiating yields

$$\frac{\partial z}{\partial \ln \Phi} \approx \left(\Phi^{1-n_\sigma} \frac{v_\phi}{c_\sigma A f_2|_{\phi=\phi_0}} \left(\frac{n_\sigma + 1}{2} \frac{\partial f_1}{\partial \phi}\bigg|_{\phi=\phi_0} \right)^{-n_\sigma} \right)^{\frac{1}{n_\sigma+1}} \tag{14.60}$$

the depth interval over which porosity decays from eϕ_0 to ϕ_0 within a porosity wave. This interval is taken here as the characteristic length scale for variations in porosity, i.e., the viscous compaction length. The derivative on the right-hand side of Eq. 14.60,

$$\frac{\partial f_1}{\partial \phi}\bigg|_{\phi=\phi_0} = \Delta\rho g \left(\frac{(1-\phi_0)}{k_0} \frac{\partial k}{\partial \phi}\bigg|_{\phi=\phi_0} - 1 \right) + \frac{v_\phi \mu}{k_0(1-\phi_0)}, \tag{14.61}$$

is zero at $v_\phi = v_\phi^{\text{crit}}$, but decreases monotonically with v_ϕ; thus dropping the first term in Eq. 14.61, substituting $v_\phi = v_\phi^{\text{crit}}$ and $\Phi = (\text{e} - 1)\ \phi_0$ in Eq. 14.60, and expanding f_2 at ϕ_0 as$(1-\phi_0) f_\phi|_{\phi=\phi_0}$yields

$$\delta = \left[\left((\text{e}-1)\phi_0 \Delta\rho g \left([1-\phi_0] \frac{\partial k}{\partial \phi}\bigg|_{\phi=\phi_0} - k_0 \right) \right)^{1-n_\sigma} \left(\frac{2k_0}{n_\sigma + 1} \right)^{n_\sigma} \frac{1}{c_\sigma A \mu f_\phi|_{\phi=\phi_0}} \right]^{\frac{1}{n_\sigma+1}}, \tag{14.62}$$

a length scale that provides a lower bound on wavelength. For a linear-viscous matrix with shear viscosity $\eta = 1/(3A)$, the constitutive relation given by Eq. 14.42, and the small-porosity limit, Eq. 14.62 simplifies to

$$\delta = \sqrt{\frac{4}{3} \frac{\eta}{\phi_0} \frac{k_0}{\mu}}$$

which, accounting for differences in the formulation of the bulk viscosity of the matrix, is identical to the viscous compaction length of McKenzie (1984). For a non-linear viscous matrix, making use of constitutive relations given by Eqs. 14.17 and 14.42, in the small-porosity limit the compaction length is

$$\delta = C \phi_0^{\frac{n_\phi - 1}{n_\sigma + 1}} \sqrt[n_\sigma+1]{\left(\frac{2}{n_\sigma + 1} \right)^{n_\sigma} \frac{c_\phi}{c_\sigma A \mu (\Delta\rho g)^{n_\sigma - 1}}}, \tag{14.63}$$

where

$$C = \sqrt[n_\sigma+1]{\left[n_\phi (\text{e}-1) \right]^{1-n_\sigma}}. \tag{14.64}$$

The factor C represents two non-general assumptions of the analysis: that the phase velocity is $n_\phi v_0$; and that the porosity decay is from $e\phi_0$ to ϕ_0. In the spirit of dimensional analysis, this factor (~2.27 for $n_\sigma = n_\phi = 3$) is neglected in the text.

References

Ague JJ, Baxter EF (2007) Brief thermal pulses during mountain building recorded by Sr diffusion in apatite and multicomponent diffusion in garnet. Earth Planet Sci Lett 261:500–516. doi:10.1016/j.epsl.2007.07.017

Ague JJ, Park J, Rye DM (1998) Regional metamorphic dehydration and seismic hazard. Geophys Res Lett 25:4221–4224

Aharonov E, Spiegelman M, Kelemen P (1997) Three-dimensional flow and reaction in porous media: implications for the earth's mantle and sedimentary basins. J Geophys Res 102:14821–14833

Ashby MF (1988) The modeling of hot isostatic pressing. In: Garvare T (ed) Proceedings hip: hot isostatic pressing – theories and applications. Centek, Lulea, pp 29–40

Athy LF (1930) Density, porosity and compaction of sedimentary rocks. Bull Am Assoc Pet Geol 14:1–24

Austrheim H (1987) Eclogitization of lower crustal granulites by fluid migration through shear zones. Earth Planet Sci Lett 81:221–232. doi:10.1016/0012-821X(87)90158-0

Barcilon V, Lovera OM (1989) Solitary waves in magma dynamics. J Fluid Mech 204:121–133

Barcilon V, Richter FM (1986) Nonlinear-waves in compacting media. J Fluid Mech 164:429–448

Bercovici D, Ricard Y, Schubert G (2001) A two-phase model for compaction and damage 1. General theory. J Geophys Res 106:8887–8906

Bouilhol P, Burg JP, Bodinier JL, Schmidt MW, Dawood H, Hussain S (2009) Magma and fluid percolation in arc to forearc mantle: evidence from Sapat (Kohistan, Northern Pakistan). Lithos 107:17–37. doi:10.1016/j.lithos.2008.07.004

Bouilhol P, Connolly JAD, Burg JP (2011) Geological evidence and modeling of melt migration by porosity waves in the sub-arc mantle of Kohistan (Pakistan). Geology 39:1091–1094. doi:10.1130/G32219.1

Cartwright I, Buick IS (1999) The flow of surface-derived fluids through alice springs age middle-crustal ductile shear zones, Reynolds Range, Central Australia. J Metamorph Geol 17:397–414

Cheadle MJ, Elliott MT, McKenzie D (2004) Percolation threshold and permeability of crystallizing igneous rocks: the importance of textural equilibrium. Geology 32:757–760. doi:10.1130/g20495.1

Connolly JAD (1997) Devolatilization-generated fluid pressure and deformation-propagated fluid flow during prograde regional metamorphism. J Geophys Res 102:18149–18173

Connolly JAD (2010) The mechanics of metamorphic fluid expulsion. Elements 6:165–172. doi:10.2113/gselements.6.3.165

Connolly JAD, Podladchikov YY (1998) Compaction-driven fluid flow in viscoelastic rock. Geodinamica Acta 11:55–84

Connolly JAD, Podladchikov YY (2000) Temperature-dependent viscoelastic compaction and compartmentalization in sedimentary basins. Tectonophysics 324:137–168

Connolly JAD, Podladchikov YY (2004) Fluid flow in compressive tectonic settings: implications for mid-crustal seismic reflectors and downward fluid migration. J Geophys Res 109:B04201. doi:10.1029/2003JB002822

Connolly JAD, Podladchikov YY (2007) Decompaction weakening and channeling instability in ductile porous media: implications for asthenospheric melt segregation. J Geophys Res 112: B10205. doi:10.1029/2005jb004213

Connolly JAD, Thompson AB (1989) Fluid and enthalpy production during regional metamorphism. Contrib Mineral Petrol 102:346–366
Connolly JAD, Schmidt MW, Solferino G, Bagdassarov N (2009) Permeability of asthenospheric mantle and melt extraction rates at mid-ocean ridges. Nature 462:209–212. doi:10.1038/nature08517
Cox SF (2005) Coupling between deformation, fluid pressures and fluid flow in ore-producing hydrothermal environments. In: Economic geology 100th anniversary volume, Denver, pp 39–75
Cox SF, Ruming K (2004) The St Ives mesothermal gold system, Western Australia – a case of golden aftershocks? J Struct Geol 26:1109–1125. doi:10.1016/j.jsg.2003.11.025
Daines MJ, Kohlstedt DL (1994) The transition from porous to channelized flow due to melt/rock reaction during melt migration. Geophys Res Lett 21:145–148
Dewey JF (2005) Orogeny can be very short. Proc Natl Acad Sci USA 102:15286–15293. doi:10.1073/pnas.0505516102
England PC, Thompson AB (1984) Pressure temperature time paths of regional metamorphism. 1. Heat-transfer during the evolution of regions of thickened continental-crust. J Petrol 25:894–928
Etheridge MA, Wall VJ, Cox SF, Vernon RH (1984) High fluid pressures during regional metamorphism and deformation – implications for mass-transport and deformation mechanisms. J Geophys Res 89:4344–4358
Ferry JM (1994) Overview of the petrologic record of fluid-flow during regional metamorphism in Northern New-England. Am J Sci 294:905–988
Ferry JM, Gerdes ML (1998) Chemically reactive fluid flow during metamorphism. Annu Rev Earth Planet Sci 26:255–287
Fulton PM, Saffer DM, Bekins BA (2009) A critical evaluation of crustal dehydration as the cause of an overpressured and weak San Andreas Fault. Earth Planet Sci Lett 284:447–454. doi:10.1016/j.epsl.2009.05.009
Gavrilenko P, Gueguen Y (1993) Fluid overpressures and pressure solution in the crust. Tectonophysics 21:91–110
Gleeson SA, Yardley BWD, Boyce AJ, Fallick AE, Munz LA (2000) From basin to basement: the movement of surface fluids into the crust. J Geochem Explor 69:527–531
Gleeson SA, Yardley BWD, Munz IA, Boyce AJ (2003) Infiltration of basinal fluids into high-grade basement, South Norway: sources and behaviour of waters and brines. Geofluids 3:33–48
Gold T, Soter S (1985) Fluid ascent through the solid lithosphere and its relation to earthquakes. Pure Appl Geophys 122:492–530
Goldschmidt VM (1954) Geochemistry. Clarendon, Oxford, p 730
Graham CM, Valley JW, Eiler JM, Wada H (1998) Timescales and mechanisms of fluid infiltration in a marble: an ion microprobe study. Contrib Mineral Petrol 132:371–389
Gratier JP, Favreau P, Renard F (2003) Modeling fluid transfer along California faults when integrating pressure solution crack sealing and compaction processes. J Geophys Res 108. doi:10.1029/2001jb000380
Gueguen Y, Palciauskas VV (1994) Introduction to the physics of rocks. Princeton University Press, Princeton, p 194
Gueguen Y, Dormieux L, Bouteca M (2004) Fundamentals of poromechanics. In: Gueguen Y, Bouteca M (eds) Mechanics of fluid-saturated rocks. Elsevier Academic, Burlington, pp 55–79
Hammer PTC, Clowes RM (1996) Seismic reflection investigations of the mount cayley bright spot: a midcrustal reflector beneath the Coast Mountains, British Columbia. J Geophys Res 101:20119–20131
Hanson RB (1997) Hydrodynamics of regional metamorphism doe to continental collision. Econ Geol Bull Soc Econ Geol 92:880–891

Hetenyi G, Cattin R, Brunet F, Bollinger L, Vergne J, Nabelek J, Diament M (2007) Density distribution of the india plate beneath the Tibetan Plateau: geophysical and petrological constraints on the kinetics of lower-crustal eclogitization. Earth Planet Sci Lett 264:226–244. doi:10.1016/j.epst.2007.09.036

Hill R (1950) The mathematical theory of plasticity. Clarendon, Oxford, p 356

Holness MB, Siklos STC (2000) The rates and extent of textural equilibration in high-temperature fluid-bearing systems. Chem Geol 162:137–153. doi:10.1016/s0009-2541(99)00124-2

Holtzman BK, Kohlstedt DL (2007) Stress-driven melt segregation and strain partitioning in partially molten rocks: effects of stress and strain. J Petrol 48:2379–2406. doi:10.1093/petrology/egm065

Huenges E, Erzinger J, Kuck J, Engeser B, Kessels W (1997) The permeable crust: geohydraulic properties down to 9101 m depth. J Geophys Res 102:18255–18265

Hunt JM (1990) Generation and migration of petroleum from abnormally pressured fluid compartments. Am Assoc Pet Geol 74:1–12

Ingebritsen SE, Manning CE (1999) Geological implications of a permeability-depth curve for the continental crust. Geology 27:1107–1110

Ingebritsen SE, Manning CE (2010) Permeability of the continental crust: dynamic variations inferred from seismicity and metamorphism. Geofluids 10:193–205. doi:10.1111/j.1468-8123.2010.00278.x

Ingebritsen SE, Sanford WE, Neuzil C (2006) Groundwater in geologic processes. Cambridge University Press, Cambridge

Jagoutz O, Muntener O, Burg JP, Ulmer P, Jagoutz E (2006) Lower continental crust formation through focused flow in km-scale melt conduits: the zoned ultramafic bodies of the Chilas complex in the Kohistan Island Arc (NW Pakistan). Earth Planet Sci Lett 242:320–342

Jiracek GR, Gonzalez VM, Caldwell TG, Wannamaker PE, Kilb D (2007) Seismogenic, electrically conductive, and fluid zones at continental plate boundaries in New Zealand, Himalaya, and California-USA. Geophys Monogr Ser 175:347–369. doi:10.1029/175GM18

Kerschhofer L, Dupas C, Liu M, Sharp TG, Durham WB, Rubie DC (1998) Polymorphic transformations between olivine, wadsleyite and ringwoodite: mechanisms of intracrystalline nucleation and the role of elastic strain. Mineral Mag 62:617–638

Kohlstedt DL, Evans B, Mackwell SJ (1995) Strength of the lithosphere – constraints imposed by laboratory experiments. J Geophys Res 100:17587–17602

Liang Y, Schiemenz A, Hesse MA, Parmentier EM, Hesthaven JS (2010) High-porosity channels for melt migration in the mantle: top is the dunite and bottom is the harzburgite and lherzolite. Geophys Res Lett 37:L15306. doi:10.1029/2010gl044162

Liotta D, Ranalli G (1999) Correlation between seismic reflectivity and rheology in extended lithosphere: southern Tuscany, Inner Northern Apennines, Italy. Tectonophysics 315:109–122

Makovsky Y, Klemperer SL (1999) Measuring the seismic properties of tibetan bright spats: evidence for free aqueous fluids in the Tibetan middle crust. J Geophys Res 104:10795–10825

Mancktelow NS (2008) Tectonic pressure: theoretical concepts and modelled examples. Lithos 103:149–177. doi:10.1016/j.lithos.2007.09.013

Manning CE, Ingebritsen SE (1999) Permeability of the continental crust: implications of geothermal data and metamorphic systems. Rev Geophys 37:127–150

McCaig AM, Wickham SM, Taylor HP (1990) Deep fluid circulation in alpine shear zones, Pyrenees, France – field and oxygen isotope studies. Contrib Mineral Petrol 106:41–60

McCuaig TC, Kerrich R (1998) P-T-t-deformation-fluid characteristics of lode gold deposits: evidence from alteration systematics. Ore Geol Rev 12:381–453

McKenzie D (1984) The generation and compaction of partially molten rock. J Petrol 2:713–765

Milke R, Abart R, Kunze K, Koch-Muller M, Schmid D, Ulmer P (2009) Matrix rheology effects on reaction rim growth i: evidence from orthopyroxene rim growth experiments. J Metamorph Geol 27:71–82. doi:10.1111/j.1525-1314.2008.00804.x

Miller SA, Collettini C, Chiaraluce L, Cocco M, Barchi M, Kaus BJP (2004) Aftershocks driven by a high-pressure CO_2 source at depth. Nature 427:724–727. doi:10.1038/nature02251

Mosenfelder JL, Connolly JAD, Rubie DC, Liu M (2000) Strength of (Mg, Fe)2SiO4 wadsleyite determined by relaxation of transformation stress. Phys Earth Planet Inter 120:63–78
Munz IA, Yardley BWD, Gleeson SA (2002) Petroleum infiltration of high-grade basement, South Norway: pressure-temperature-time-composition (P-T-t-X) constraints. Geofluids 2:41–53
Nabelek PI (2009) Numerical simulation of kinetically-controlled calc-silicate reactions and fluid flow with transient permeability around crystallizing plutons. Am J Sci 309:517–548. doi:10.2475/07.2009.01
Nakashima Y (1995) Transport model of buoyant metamorphic fluid by hydrofracturing in leaky rock. J Metamorph Geol 13:727–736
Neuzil CE (1994) How permeable are clays and shales? Water Resour Res 30:145–150
Norton D, Knapp R (1977) Transport phenomena in hydrothermal systems – nature of porosity. Am J Sci 277:913–936
Okamoto A, Tsuchiya N (2009) Velocity of vertical fluid ascent within vein-forming fractures. Geology 37:563–566. doi:10.1130/g25680a.1
Oliver GJH, Chen F, Buchwaldt R, Hegner E (2000) Fast tectonometamorphism and exhumation in the type area of the Barrovian and Buchan zones. Geology 28:459–462
Ozel O, Iwasaki T, Moriya T, Sakai S, Maeda T, Piao C, Yoshii T, Tsukada S, Ito A, Suzuki M, Yamazaki A, Miyamachi H (1999) Crustal structure of Central Japan and its petrological implications. Geophys J Int 138:257–274
Padron-Navarta JA, Tommasi A, Garrido CJ, Sanchez-Vizcaino VL, Gomez-Pugnaire MT, Jabaloy A, Vauchez A (2010) Fluid transfer into the wedge controlled by high-pressure hydrofracturing in the cold top-slab mantle. Earth Planet Sci Lett 297:271–286. doi:10.1016/j.epsl.2010.06.029
Padron-Navarta JA, Sanchez-Vizcaino VL, Garrido CJ, Gomez-Pugnaire MT (2011) Metamorphic record of high-pressure dehydration of antigorite serpentinite to chlorite harzburgite in a subduction setting (Cerro del Almirez, Nevado-Filabride Complex, Southern Spain). J Petrol 52:2047–2078. doi:10.1093/petrology/egr039
Paterson MS, Luan FC (1990) Quartzite rheology under geological conditions. In: Knipe RJ, Rutter EH (eds) Deformation mechanisms, rheology and tectonics, vol 54. The Geological Society, London, pp 299–307
Peng ZG, Vidale JE, Creager KC, Rubinstein JL, Gomberg J, Bodin P (2008) Strong tremor near Parkfield, CA, excited by the 2002 Denali fault earthquake. Geophys Res Lett 35. doi:10.1029/2008gl036080
Petrini K, Podladchikov Y (2000) Lithospheric pressure-depth relationship in compressive regions of thickened crust. J Metamorph Geol 18:67–78
Plank T, Langmuir CH (1998) The chemical composition of subducting sediment and its consequences for the crust and mantle. Chem Geol 145:325–394
Powley DE (1990) Pressures and hydrogeology in petroleum basins. Earth Sci Rev 29:215–226
Price JD, Wark DA, Watson EB, Smith AM (2006) Grain-scale permeabilities of faceted polycrystalline aggregates. Geofluids 6:302–318. doi:10.1111/j.1468-8123.2006.00149.x
Ranalli G (1995) Rheology of the earth. Springer, New York
Ranalli G, Rybach L (2005) Heat flow, heat transfer and lithosphere rheology in geothermal areas: features and examples. J Volcanol Geotherm Res 148:3–19. doi:10.1016/j.jvolgeores.2005.04.010
Read CM, Cartwright I (2000) Meteoric fluid infiltration in the middle crust during shearing: examples from the Arunta Inlier, Central Australia. J Geochem Explor 69:333–337
Rice JR (1992) Fault stress states, pore pressure distributions, and the weakness of the San Andreas Fault. In: Evans B, Wong T-F (eds) Fault mechanics and transport properties of rocks. Academic, New York, pp 475–503
Richter FM, McKenzie D (1984) Dynamical models for melt segregation from a deformable rock matrix. J Geol 92:729–740
Rozhko AY, Podladchikov YY, Renard F (2007) Failure patterns caused by localized rise in pore-fluid overpressure and effective strength of rocks. Geophys Res Lett 34:L22304. doi:10.1029/2007gl031696

Rubie DC, Thompson AB (1985) Kinetics of metamorphic reactions. In: Thompson AB, Rubie DC (eds) Metamorphic reactions kinetics, textures, and deformation, vol 4. Springer, New York, pp 291

Rubin RM (1995) Propagation of magma-filled cracks. Annu Rev Earth Planet Sci 23:287–336

Rubinstein JL, Vidale JE, Gomberg J, Bodin P, Creager KC, Malone SD (2007) Non-volcanic tremor driven by large transient shear stresses. Nature 448:579–582. doi:10.1038/nature06017

Rutter EH (1983) Pressure solution in nature, theory and experiment. J Geol Soc Lond 140:725–740

Scarpa R, Amoruso A, Crescentini L, Fischione C, Formisano LA, La Rocca M, Tronca F (2008) Slow earthquakes and low frequency tremor along the Apennines, Italy. Ann Geophys 51:527–538

Schmalholz SM, Podladchikov Y (1999) Buckling versus folding: importance of viscoelasticity. Geophys Res Lett 26:2641–2644

Scholz CH (1988) The brittle-plastic transition and the depth of seismic faulting. Geol Rundsch 77:319–328

Scott DR (1988) The competition between percolation and circulation in a deformable porous-medium. J Geophys Res 93:6451–6462

Scott DR, Stevenson DJ (1986) Magma ascent by porous flow. J Geophys Res 91:9283–9296

Scott DR, Stevenson DJ, Whitehead JA (1986) Observations of solitary waves in a viscously deformable pipe. Nature 319:759–761

Shaw DM (1956) Geochemistry of pelite rocks, iii, major elements and general geochemistry. Geol Soc Am Bull 67:919–934

Shimizu I (1995) Kinetics of pressure solution creep in quartz; theoretical considerations. Tectonophysics 245:121–134

Sibson RH (1986) Earthquakes and rock deformation in crustal fault zones. Annu Rev Earth Planet Sci 14:149–175

Sibson RH (1992) Fault-valve behavior and the hydrostatic lithostatic fluid pressure interface. Earth Sci Rev 32:141–144

Sibson RH (2000) Tectonic controls on maximum sustainable overpressure: fluid redistribution from stress transitions. J Geochem Explor 69:471–475

Sibson RH (2004) Controls on maximum fluid overpressure defining conditions for mesozonal mineralisation. J Struct Geol 26:1127–1136. doi:10.1016/j.jsg.2003.11.003

Sibson RH (2009) Rupturing in overpressured crust during compressional inversion-the case from NE Honshu, Japan. Tectonophysics 473:404–416. doi:10.1016/j.tecto.2009.03.016

Simpson GDH (1998) Dehydration-related deformation during regional metamorphism, NW Sardinia, Italy. J Metamorph Geol 16:457–472

Skelton ADL (1996) The timing and direction of metamorphic fluid flow in Vermont. Contrib Mineral Petrol 125:75–84

Skelton ADL, Valley JW, Graham CM, Bickle MJ, Fallick AE (2000) The correlation of reaction and isotope fronts and the mechanism of metamorphic fluid flow. Contrib Mineral Petrol 138:364–375

Spiegelman M (1993) Flow in deformable porous-media. 1. Simple analysis. J Fluid Mech 247:17–38

Spiegelman M, Elliott T (1993) Consequences of melt transport for uranium series disequilibrium in young lavas. Earth Planet Sci Lett 118:1–20

Spiegelman M, Kelemen PB, Aharonov E (2001) Causes and consequences of flow organization during melt transport: the reaction infiltration instability in compactible media. J Geophys Res 106:2061–2077

Spiers CJ, Schutjens PMTM (1990) Densification of crystalline aggregates by diffusional creep. J Geolo Soc Spec Publ 54:215–227

Stahle HJ, Raith M, Hoernes S, Delfs A (1987) Element mobility during incipient granulite formation at kabbaldurga, Southern India. J Petrol 28:803–834

Staude S, Bons PD, Markl G (2009) Hydrothermal vein formation by extension-driven dewatering of the middle crust: an example from SW Germany. Earth Planet Sci Lett 286:387–395. doi:10.1016/j.epsl.2009.07.012

Stern T, Kleffmann S, Okaya D, Scherwath M, Bannister S (2001) Low seismic-wave speeds and enhanced fluid pressure beneath the Southern Alps of New Zealand. Geology 29:679–682

Stevenson D (1989) Spontaneous small-scale melt segregation in partial melts undergoing deformation. Geophys Res Lett 16:1067–1070

Suetnova EI, Carbonell R, Smithson SB (1994) Bright seismic reflections and fluid movement by porous flow in the lower crust. Earth Planet Sci Lett 126:161–169. doi:10.1016/0012-821x(94)90248-8

Sumita I, Yoshida S, Kumazawa M, Hamano Y (1996) A model for sedimentary compaction of a viscous medium and its application to inner-core growth. Geophys J Int 124:502–524

Tenthorey E, Cox SF (2006) Cohesive strengthening of fault zones during the interseismic period: an experimental study. J Geophys Res 111:B09202. doi:10.1029/2005jb004122

Thompson AB, Connolly JAD (1990) Metamorphic fluids and anomalous porosities in the lower crust. Tectonophysics 182:47–55

Tumarkina E, Misra S, Burlini L, Connolly JAD (2011) An experimental study of the role of shear deformation on partial melting of a synthetic metapelite. Tectonophysics 503:92–99. doi:10.1016/j.tecto.2010.12.004

Upton P, Koons PO, Chamberlain CP (1995) Penetration of deformation-driven meteoric water into ductile rocks: isotopic and model observations from the Southern Alps, New Zealand. N Z J Geol Geophys 38:535–543

van Haren JLM, Ague JJ, Rye DM (1996) Oxygen isotope record of fluid infiltration and mass transfer during regional metamorphism of pelitic schist, Connecticut, USA. Geochim et Cosmochim Acta 60:3487–3504

Vanyan LL, Gliko AO (1999) Seismic and electromagnetic evidence of dehydration as a free water source in the reactivated crust. Geophys J Int 137:159–162

Vrijmoed JC, Podladchikov YY, Andersen TB, Hartz EH (2009) An alternative model for ultra-high pressure in the Svartberget Fe-Ti Garnet-Peridotite, Western Gneiss Region, Norway. Eur J Mineral 21:1119–1133. doi:10.1127/0935-1221/2009/0021-1985

Walther JV, Orville PM (1982) Volatile production and transport in regional metamorphism. Contrib Mineral Petrol 79:252–257

Wark DA, Watson EB (1998) Grain-scale permeabilities of texturally equilibrated, monomineralic rocks. Earth Planet Sci Lett 164:591–605

Warren CJ, Smye AJ, Kelley SP, Sherlock SC (2011) Using white mica $^{40}Ar/^{39}Ar$ data as a tracer for fluid flow and permeability under high-p conditions: Tauern Window, Eastern Alps. J Metamorph Geol. doi:10.1111/j.1525-1314.2011.00956.x

Wickham SM, Peters MT, Fricke HC, Oneil JR (1993) Identification of magmatic and meteoric fluid sources and upward-moving and downward-moving infiltration fronts in a metamorphic core complex. Geology 21:81–84

Wiggins C, Spiegelman M (1995) Magma migration and magmatic solitary waves in 3-d. Geophys Res Lett 22:1289–1292

Wilkinson DS, Ashby MF (1975) Pressure sintering by power law creep. Acta Metall 23:1277–1285

Wing BA, Ferry JM (2007) Magnitude and geometry of reactive fluid flow from direct inversion of spatial patterns of geochemical alteration. Am J Sci 307:793–832. doi:10.2475/05.2007.02

Wong TF, Christian D, Menendez B (2004) Mechanical compaction. In: Gueguen Y, Bouteca M (eds) Mechanics of fluid-saturated rocks. Elsevier Academic, Burlington, pp 55–79

Xiao XH, Evans B, Bernabe Y (2006) Permeability evolution during non-linear viscous creep of calcite rocks. Pure Appl Geophys 163:2071–2102. doi:10.1007/s00024-006-0115-1

Yardley BWD (1983) Quartz veins and devolatilization during metamorphism. J Geol Soc 140:657–663

Yardley B, Gleeson S, Bruce S, Banks D (2000) Origin of retrograde fluids in metamorphic rocks. J Geochem Explor 69:281–285

Young ED, Rumble D (1993) The origin of correlated variations in insitu O^{18}/O^{16} and elemental concentrations in metamorphic garnet from southeastern Vermont, USA. Geochim et Cosmochim Acta 57:2585–2597. doi:10.1016/0016-7037(93)90419-w

Zharikov AV, Vitovtova VM, Shmonov VM, Grafchikov AA (2003) Permeability of the rocks from the Kola superdeep borehole at high temperature and pressure: implication to fluid dynamics in the continental crust. Tectonophysics 370:177–191. doi:10.1016/s0040-1951(03)00185-9

Zhu W, David C, T-f W (1995) Network modeling of permeability evolution during cementation and hot isostatic pressing. J Geophys Res 100:15451–15464

Zhu W, Evans B, Bernabe Y (1999) Densification and permeability reduction in hot-pressed calcite: a kinetic model. J Geophys Res 104:25501–25511

Zoback MD, Townend J (2001) Implications of hydrostatic pore pressures and high crustal strength for the deformation of intraplate lithosphere. Tectonophysics 336:19–30